Alma Mater Studiorum · Università di Bologna

SCHOOL OF
ENGINEERING AND ARCHITECTURE
- Forlí Campus -

Master's Degree in Aerospace Engineering

class LM20

Graduation Thesis in:
Experimental methods in aerodynamics

Heat-transfer enhancement in turbulent pipe flow with pulsed-jet actuators

Candidate :
Marco Bocconcelli

Supervisor :
Prof. Gabriele Bellani

Co-Supervisor :
Lorenzo Magnani

Session III
Academic Year 2023/2024

Abstract

The convective heat-transfer enhancement in a fully turbulent pipe flow employing a pulsed, slot jet in crossflow is investigated experimentally.
Heat-exchange is critical in numerous industrial applications, impacting the efficiency, performance, and safety of systems ranging from power generation to electronics cooling and aerospace engineering.
Convection, particularly in turbulent flows, plays a crucial role in heat-transfer enhancement. Active flow control techniques, such as pulsed-jets, have been explored to enhance convective heat-transfer. However, many existing studies are limited to low Reynolds numbers, limiting their applicability to industrial processes operating at higher Reynolds numbers.
The effectiveness of active flow control techniques for heat-transfer enhancement in a high Reynolds number facility, specifically the CICLoPE wind tunnel, is assessed. The study involves developing an impinging jet in crossflow, controlled by frequency and duty cycle, and assessing its impact on convective heat-transfer using infrared thermography on a printed circuit board modelled as a heated thin-foil sensor.

Keywords: Heat-transfer enhancement, Convection, Infrared thermography, Pipe flow, Pulsed-jet in crossflow

Contents

List of Tables

List of Figures

List of Symbols

α	Thermal diffusivity
β	Thermal expansion coefficient
λ	Thermal conductivity of the material
μ	Dynamic viscosity
∇	Nabla operator
ν	Kinematic viscosity
ρ	Density
σ	Stefan-Boltzmann constant
τ	Viscous stress tensor
τ_{wall}	Wall shear stress
ε	Emissivity
Bi	Biot number
Cf	Skin friction coefficient
d, D	Representative dimension of the problem
DC	Duty cycle

f Body forces per unit mass

f Pulsation frequency

g Gravitational acceleration

Gr Grashof number

h Convective heat-transfer coefficient

K von Karman constant

k Thermal conductivity of the fluid

l^* Length scale in inner units

M Mach number

Nu Nusselt number

p Pressure

Pr Prandtl number

Q Heat introduced in unit time

q Heat flux

q_c Convective heat flux

q_j Heat flux by Joule effect

q_{cond} Conductive heat flux

q_{rad} Radiative heat flux

R Velocity Ratio

Ra Rayleigh number

Re Reynolds number

Re_τ Friction Reynolds number

T Temperature

T_∞ Bulk temperature

T_s Temperature of the surface

$u(x, y, z, t)$ Fluctuating value of a random variable

U^+ Inner-scaled velocity

U_∞ free-stream velocity

u_τ Friction velocity

Chapter 1

Introduction

This thesis aims to assess the effectiveness of an active flow control technique, namely an impinging jet in crossflow, on convective heat-transfer enhancement.
heat-exchange is a fundamental process in numerous industrial applications, where the transfer of thermal energy is critical for the efficiency, performance and safety of various systems. Effective heat-exchange mechanisms are essential in applications ranging from power generation to electronics cooling, and aerospace engineering.
As a matter of fact, the thermal efficiency of gas turbine engines is directly correlated with the turbine inlet temperature: as a matter of fact, higher turbine inlet temperatures result in improved efficiency. This temperature, however, is constrained by the material properties of the turbine blades, which must withstand extreme conditions without degrading. Therefore, to improve the efficiency, we can either act on material properties or act on the flow using active cooling techniques. Improved cooling can result in efficiency gains of up to 3-4 % in modern gas turbine engines [1]. Even a few percentage points in efficiency increase would represent a significant leap forward, considering that fuel is the biggest operating cost for airlines. This improvement could lead to substantial financial savings and reduced environmental impact for the aviation industry.
Furthermore, in the electronics industry, managing the heat generated by electronic components is vital to ensure the reliability and longevity of devices. As electronic devices become more compact and powerful, the heat they generate increases, mak-

ing effective thermal management even more challenging. Poor heat dissipation can lead to overheating, which can cause component failure, reduce the lifespan of devices and limit the performance of high-speed microchips. Advanced cooling techniques are, therefore, essential to maintain optimal operating temperatures and preventing thermal damages.

Convection plays a crucial role in heat-transfer and it is the most commonly used mechanism for enhancing cooling in both industrial and research activities. Its effectiveness is strongly influenced by the flow characteristics, particularly turbulence, which significantly increases heat and mass transfer performance. Moreover, in many industrial applications, the flow is typically turbulent. Turbulent flows are characterized by chaotic, irregular fluid motion, which leads to increased mixing and a higher rate of heat-transfer compared to laminar flows.

Active flow control techniques have been explored to enhance convective heat-transfer. One notable example is the work of Castellanos et al.[2], who conducted a parametric study on an impinging jet in a crossflow to identify specific control actions that increase convective heat-transfer in a turbulent boundary layer. However, their experiments were performed at relatively low Reynolds numbers, which limits their direct applicability to many industrial processes that operate at much higher Reynolds numbers.

This thesis aims to validate the effectiveness of active flow control techniques for heat-transfer enhancement in a high Reynolds number facility, specifically the CICLoPE wind tunnel. To study the convective heat-transfer enhancement an impinging jet in crossflow, controlled in terms of frequency and duty cycle, is tested. The effectiveness of the control action has been quantified by applying infrared thermography to assess heat fluxes over a heated test surface.

1.1 Thesis objective

This thesis aims to assess the effectiveness of an impinging jet in crossflow for enhancing convective heat-transfer. This will be achieved by measuring the heat-transfer over a heated thin-foil sensor, with infrared thermography used as the pri-

mary method for capturing temperature distributions and estimating the change in cooling performances.

1.2 Thesis outline

First of all, a theoretical background, in which the mathematical and theoretical explanation of all the topics that will be treated in this dissertation is given to the reader to have a better comprehension of this thesis.
Then, the reader will find a chapter related to the description of the facility (i.e. CICLoPE wind tunnel) in which the experiments were carried out with its unique characteristics.
The following chapter provides a detailed overview of all the experimental instruments used in this thesis, along with the underlying principles of the data acquisition procedure.
The thesis proceeds with presenting and discussing all the experimental results collected to characterize the output flow of the jet and evaluate its effect on the enhancement of convective heat-transfer.
Lastly, the conclusions and some remarks for future works to improve the setup performances.

Chapter 2

Theoretical Background

2.1 Fluid dynamics background

Fluid dynamics is the branch of physics that studies the movement of fluids, it plays a crucial role in numerous engineering fields such as aerospace, automotive, and civil engineering, among many others.
The governing equations of fluid dynamics are the Navier-Stokes equations, consisting of a set of partial differential equations derived from Newton's second law of motion and the conservation principles of mass and momentum. The Navier-Stokes equations for an incompressible, Newtonian fluid written in Eulerian form and neglecting body forces can be written as follows:

$$\nabla \cdot \mathbf{U} = 0 \tag{2.1}$$

$$\frac{\partial \mathbf{U}}{\partial t} + (\mathbf{U} \cdot \nabla)\mathbf{U} = -\frac{1}{\rho}\nabla p + \nu \nabla^2 \mathbf{U} \tag{2.2}$$

Where $\mathbf{U} = (U, V, W)$ is the velocity vector, ρ is the density, p is the pressure, and ν is the kinematic viscosity. Equation 2.1, known as the continuity equation, is derived from the principle of mass conservation. Meanwhile, equation 2.2 represents the momentum balance equation, originating from Newton's second law and it is

composed of four terms:

1. **Unsteady term:**

$$\frac{\partial U}{\partial t} \tag{2.3}$$

This term represents the change in momentum due to the unsteady flow.

2. **Convective term:**

$$(U \cdot \nabla)U \tag{2.4}$$

This term accounts for the change in momentum due to the movement of the fluid itself.

3. **Pressure gradient term:**

$$-\frac{1}{\rho}\nabla p \tag{2.5}$$

This term represents the effect of pressure forces on the fluid.

4. **Viscous term:**

$$\nu\nabla^2 U \tag{2.6}$$

This term accounts for the viscous forces within the fluid.
Solving the Navier-Stokes equations analytically is feasible only for simple cases due to their non-linearity, which precludes the use of many mathematical methods that rely on linearity. Most practical problems require numerical methods to solve them.

2.1.1 Turbulent flows and RANS

Although turbulence is a common phenomenon, it lacks a coherent definition. However, to classify a flow as turbulent it should exhibit all of the following characteristics:

- Disordered motion: Never reproducible in full detail, no analytical solution of the governing equations;
- High Reynolds numbers;
- 3-D fluctuations of the velocity field;

- Momentum, mass and heat-transfer are enhanced.

One of the distinctive characteristics of turbulent flows is the existence of a wide range of different scale eddies. The largest scales are typically linked to the macroscopic geometric features of the flow; in the case of pipe flow, this corresponds to the pipe radius R. The energy associated with the turbulent motion comes from the biggest scales, which get their energy from the mean flow throughout a production mechanism. Then, the energy is transferred in an inviscid way to scales gradually smaller until it is dissipated into heat at small scales by viscous forces.
A length scale, a time scale, and a velocity scale characterize the scales. For large scales, the length scale is determined by the flow geometry (R), and the velocity scale can be associated with the mean velocity of the flow (U). As the cascade mechanism continues, these large eddies break up, and their dimensions decrease until the local Reynolds number approaches 1. Thus, $Re = 1$ sets the size of the smallest scales (η); beyond this point, viscosity acts, dissipating the energy into heat. Consequently, the smallest scales can be considered isotropic because any macroscopic information is lost in the cascade process. In other words, the smallest scales are "universal".
In a turbulent flow, the velocity U(x,t) can be considered as a random variable, therefore it is necessary to apply the Reynolds decomposition:

$$U(x,t) = \bar{U}(x,t) + u(x,t) \tag{2.7}$$

$$P(x,t) = \bar{P}(x,t) + p(x,t) \tag{2.8}$$

Where the instantaneous velocity U(x,t) and pressure P(x,t) are split into their mean (denoted by capital letters with an overlaying bar) and fluctuating part (denoted by small letters). Applying the Reynolds decomposition to the Navier-Stokes equations, the so-called Reynolds averaged Navier-Stokes equations (RANS) can be obtained. The RANS differs from the traditional Naveir-Stokes in two ways: all instantaneous quantities are exchanged with mean quantities and there is one additional term that arises from the non-linearity of the convective term.
The equations can be specialized for the case of a circular pipe with radius R. It is

convenient to define a cylindrical coordinate system (x, r, θ), where x represents the axial coordinate, r denotes the radial coordinate (originating from the pipe centerline and perpendicular to the wall), and θ is the angular coordinate.
Considering that a turbulent pipe flow is statistically axial-symmetric:

$$\overline{W} = \overline{uw} = \overline{v} = \frac{\partial}{\partial \theta} \tag{2.9}$$

Substituting into the RANS equations:

$$\frac{\partial \overline{U}}{\partial x} + \frac{1}{r}\frac{\partial}{\partial \theta}(r\overline{V}) = 0 \tag{2.10}$$

$$\frac{\partial \overline{U}}{\partial t} + \overline{U}\frac{\partial \overline{U}}{\partial x} + \overline{V}\frac{\partial \overline{U}}{\partial r} = -\frac{1}{\rho}\frac{\partial \overline{p}}{\partial x} - \frac{\partial}{\partial x}\overline{u}^2 - \frac{1}{r}\frac{\partial}{\partial r}(r\overline{uv}) + \nu\nabla^2\overline{U} \tag{2.11}$$

$$\frac{\partial \overline{V}}{\partial t} + \overline{U}\frac{\partial \overline{V}}{\partial x} + \overline{V}\frac{\partial \overline{V}}{\partial r} = -\frac{1}{\rho}\frac{\partial \overline{p}}{\partial r} - \frac{\partial}{\partial x}\overline{uv} - \frac{1}{r}\frac{\partial}{\partial r}(r\overline{v}^2) + \overline{w}^2\frac{1}{r} + \nu\left(\nabla^2\overline{V} - \frac{\overline{V}}{r^2}\right) \tag{2.12}$$

Then, with the additional hypothesis of statistically stationary and fully-developed flow, we can obtain the following relations:

$$\frac{\partial}{\partial t} = 0, \quad \frac{\partial \overline{U}}{\partial x} = \frac{\partial \overline{u}^2}{\partial x} = \frac{\partial \overline{v}^2}{\partial x} = 0 \tag{2.13}$$

Taking into account the no-slip boundary condition and axial symmetry, where $\overline{V}\big|_{r=R} = \overline{V}\big|_{r=0} = 0$, and considering the continuity equation, we can say that the mean wall-normal velocity must be zero across the entire profile:

$$\overline{V} = 0 \quad \text{and} \quad \frac{\partial \overline{U}}{\partial x} = 0 \tag{2.14}$$

$$\frac{1}{\rho}\frac{\partial \overline{p}}{\partial r} + \frac{\partial \overline{v}^2}{\partial r} = \frac{\overline{w}^2}{r} - \frac{\overline{v}^2}{r} \tag{2.15}$$

Integrating between a generic radial r and the radius R we get:

$$\frac{1}{\rho}(\overline{p}_w - \overline{p}) - \overline{v}^2 = \int_r^R \left(\frac{\overline{w}^2}{r} - \frac{\overline{v}^2}{r}\right) dr \tag{2.16}$$

The quantities with the subscript 'w' represent the values of those quantities at the wall, then deriving over x, and using the hypothesis of fully-developed flow:

$$\frac{\partial \overline{p}}{\partial x} = \frac{\partial \overline{p}_w}{\partial x} \tag{2.17}$$

Equation 2.17 states that the axial pressure gradient is uniform along the pipe radius. Substituting in the x component of the momentum equation:

$$\frac{1}{\rho}\frac{d\overline{p}_w}{dx} = -\frac{1}{r}\frac{d}{dr}(r\overline{uv}) + \nu\frac{1}{r}\frac{d}{dr}\left(r\frac{d\overline{U}}{dr}\right) \tag{2.18}$$

Introducing the definition of wall shear stress:

$$\tau = \mu\frac{\partial \overline{U}}{\partial r} \tag{2.19}$$

We get:

$$\frac{d\overline{p}_w}{dx} = -\frac{1}{r}\frac{d(r\tau)}{dr} \tag{2.20}$$

Integrating between 0 and R:

$$\tau_w = \frac{R}{2}\frac{d\overline{p}_w}{dx} \tag{2.21}$$

This equation correlates the pressure drop throughout the pipe and the wall shear stress, this relation above is crucial in experimental studies of pipe flows. If we integrate up to a generic radius r instead of R, and introduce the variable $y = R - r$ (the wall-normal distance), we obtain the general relationship:

$$\tau(y) = \tau_w\left(1 - \frac{y}{R}\right) \tag{2.22}$$

This represents a linear relationship, decreasing from the wall where $\tau = \tau_w$, to the centerline where $\tau = 0$.

2.1.2 Wall-bounded flows

Turbulence can be divided into free-shear flows such as jets or wakes and wall-bounded flows as the channel, boundary layer or pipe flow. In free shear flows, turbulence originates from velocity differences within the flow field. In contrast, wall turbulence is initiated by the presence of a solid surface, the fluid's viscosity, and the resulting no-slip condition (where the fluid velocity at the wall is zero). In a thin region near the wall, the viscous forces become important and the gradient is much larger than the corresponding laminar situation. This highlights a defining characteristic of wall-bounded turbulent flows: the existence of two distinct layers, each with its unique length scale.
Some of the prominent features of wall-bounded flows are the following:

- Two-layer character: Two length scales determining the inner and outer layer thicknesses;
- Complex turbulence structure;
- Highly anisotropic turbulence;
- Strong inhomogeneity in terms of length scales and fluctuation intensities;
- Strong near-wall turbulence production.

According to the standard analysis, wall-bounded turbulent flows can be divided into two regions: an inner region close to the wall, and an outer region far away from the wall. The assumption made is that in the inner region, viscous forces heavily influence the dynamics of the flow, while the external geometry does not influence the flow behaviour; according to this hypothesis, all turbulent flows should display a similar near-wall behaviour even if their external conditions are different. While in the outer region, the fluid dynamics is dominated by inertial forces.

wall-bounded turbulent scaling

To achieve a correct self-similar description of wall-bounded flows, it is essential to establish one velocity scale and one length scale for both the inner and outer

regions. For the outer region, the velocity at the centerline U_0 and the characteristic dimension of the geometry δ can be used. Inside this region, any information about the viscosity is lost and therefore the deflect velocity is only a function of outer scale distances, the scaling law is the so-called "defect law", proposed by Von Karman. For the inner region, the "law of the wall" scaling applies (introduced by Prandtl) based on the assumption that the flow has lost any information about the larger scales. In this region, the variables that influence the mean velocity are the wall shear stress τ, the wall-normal distance y, and the kinematic viscosity ν. Thus, we define the friction velocity, the characteristic velocity scale in this region, as:

$$u_\tau = \sqrt{\frac{\tau_w}{\rho}} \tag{2.23}$$

Where ρ is the density of the fluid, then we introduce also the viscous length, the characteristic length scale of the inner region, defined as:

$$l^* = \frac{\nu}{u_\tau} \tag{2.24}$$

Using both equations we can define the viscous time scale:

$$t^* = \frac{l^*}{u_\tau} = \frac{\nu}{u_\tau^2} \tag{2.25}$$

We can define a characteristic Reynolds number for wall-bounded flows, called friction Reynolds number which, in the case of a pipe flow, is equal to the pipe radius normalized in inner variables:

$$Re_\tau = \frac{Ru_\tau}{\nu} = \frac{R}{l^*} = R^+ \tag{2.26}$$

Where the superscript + denotes inner scaled variables, then using equations 2.23 and 2.24 we normalize with inner variables the mean velocity and the wall-normal distance:

$$U^+ = \frac{\overline{U}}{u_\tau}, \quad y^+ = \frac{y}{l^*} \tag{2.27}$$

Applying 2.27 to the momentum equation for turbulent wall-bounded flows we obtain the inner-scaled momentum equation:

$$1 - \frac{y^+}{h^+} = \frac{\partial U^+}{\partial y^+} - \langle uv \rangle^+ \tag{2.28}$$

This equation allows to subdivide wall-bounded flows into several layers each with peculiar characteristics:

- Viscous sublayer: It is the layer closer to the wall, here the effects of viscosity are dominant, and the viscous stresses and much larger than the Reynolds shear stresses. Defined in inner units in the following range $0 \leq y^+ \leq 5$;

- Buffer layer: In this layer, the Reynolds shear stresses are of the same order of magnitude as the viscous stresses. It extends in inner units in the range $5 < y^+ \leq 100$;

- Overlap layer: In this layer, the Reynolds shear stresses are much larger than the viscous ones. In inner units, it is characterized by the range $100 < y^+ \leq 0.1\delta$ where δ is the outer unit of the specific wall-bounded flow, for a pipe flow δ is the pipe radius R,

- Core region: Completely belongs to the outer region in which the inertial forces are dominant, it extends from 0.1δ up to the centerline.

In the overlap region, for large Reynolds numbers, there is an overlap of the inner and outer layers on which both scaling laws (i.e. Law of the wall and defect law) apply, The combination of these two produces the logarithmic law:

$$U^+ = \frac{1}{K} \ln y^+ + B \tag{2.29}$$

Where K is the Karman constant and B is a constant that depends on geometry and flow characteristics.

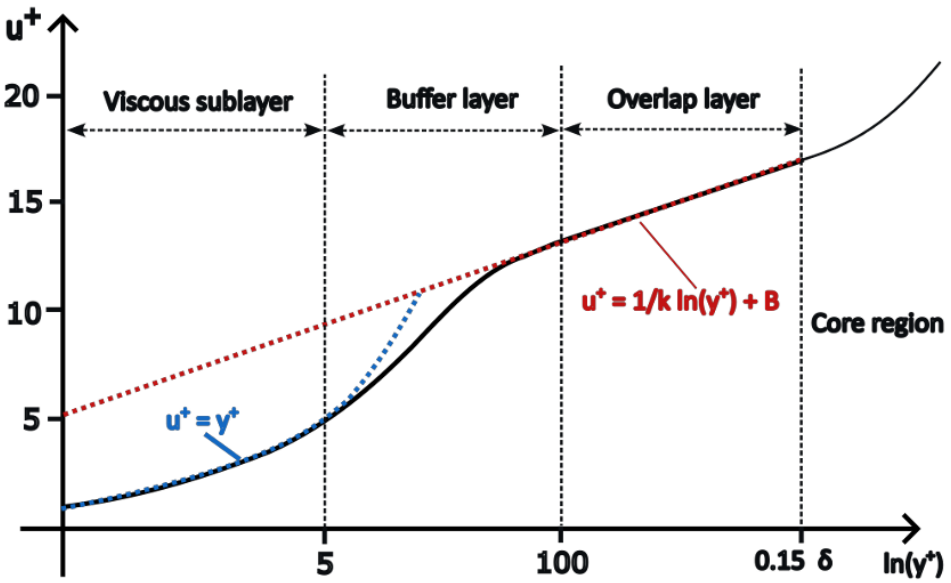

Figure 2.1: Logarithmic law,[3].

2.1.3 Jets in crossflow

This thesis aims to assess the convective heat-transfer enhancement provided by impinging jet in crossflow, which is an active flow control method. The impinging jet excites the structure and the organization of large-scale turbulence, and an increment in convection capabilities is obtained, as demonstrated by Kataoka et al [4].
The transverse jet in crossflow used in this thesis is characterized by a counter-rotating vortex pair that forms downstream of the jet [5]. This vortex motion strongly influences the velocity and temperature distributions downstream of the jet. As stated by Fric and Roshko [6] and Kelso [7], four different types of coherent structures are present in the near field of the jet:

- Counter-rotating vortex pair (CVP)

- Shear-layer vortices which are predominant in the initial portion of the jet;

- A system of horseshoe vortices wrapped around the base of the jet;

- Wake vortices extending from the wall to the jet.

The formation and interaction of these coherent structures, both among themselves and with the main flow, have been thoroughly investigated [8] and linked to the increased mixing efficiency of crossflow jets [9, 10]. Broadwell and Breidenthal [10] assert that the jet mixing rate becomes independent of the Reynolds number above a critical value. Although most of the studies on jets in crossflow are focused on round jets, there are several contributions (see e.g. [11, 12]) describing that the characteristic structures and mixing characteristics are not widely affected by the shape of the injected jet.

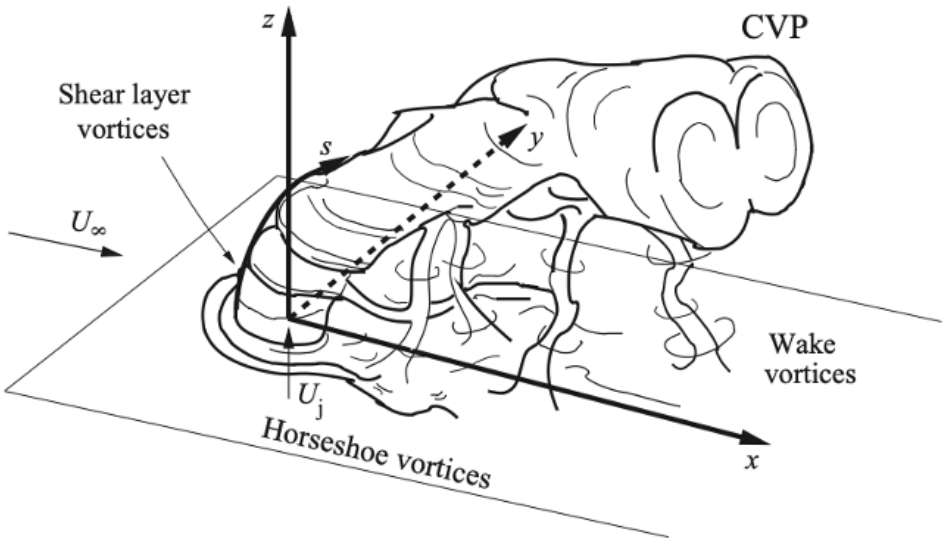

Figure 2.2: Schematic of the coherent structures of a jet in crossflow,[13].

Several studies were conducted to understand which parameters affect the jet coherent structures and the mixing properties. The jet mixing rate is affected by the

velocity ratio between the crossflow and the jet:

$$R = \frac{U_j}{U_\infty} \tag{2.30}$$

The velocity ratio affects the penetration and bending of the injected flow and determines the extent of the wake region formed on the lee of the jet, where small velocity gradients and lower mixing are present [14].
Adding pulsation is one way to improve the transport efficiency of jets in crossflow. Studies by Mladin and Zumbrunnen [15] and Liu and Sullivan [16], report that pulsating an impinging jet can either increase or decrease its heat-transfer capabilities, depending on the actuation frequency. Specifically, pulsation at the jet's natural frequency has been found to enhance the eddies size, thereby improving heat-exchange near the wall [17]. Eroglu and Breidenthal [18] investigated the effects of jet pulsation on vortical structure: they found that jets excited by square waves produce distinct vortex rings.
When the jet flow is excited the size of the mixing area, penetration depth, and overall mixing can be increased [19]. However, the specific pulsation frequencies required for optimal performance vary widely and are heavily influenced by the apparatus used, indicating that the objective function for optimization is not universal [20].
Johari et al. [21] studied the mixing properties of fully-modulated (valve-actuated) turbulent jets in crossflow. It was found that both the frequency and duty cycle of the actuation influence the mixing properties. To summarize, several parameters such as frequency, duty cycle, and velocity ratio affect the enhancement of mixing and heat-transfer.
In the experiment conducted by Castellanos et al.[2] they use a rectangular jet and find out that the best absolute performance happens to be for a duty cycle of 75% and a pulsation frequency of 225 Hz. But including the efficiency estimation based on the volumetric flow rate injected the best control action is the one with the lowest duty cycle. This occurs because the duty cycle is closely associated with the amount of fluid being injected.

2.2 Velocity measurements background

2.2.1 Hot-wire anemometry

During the test and validation campaigns of the jet, the acquisition of the velocity signal was performed by using a hot-wire anemometer. A hot-wire anemometer is made of a piece of thin, electrically heated wire made of a conductive material (e.g. tungsten, platinum, or a platinum-iridium alloy), inserted into the flow. The typical diameter of the wire is $5\mu m$. At equilibrium, the heat provided by the Joule effect must be balanced by heat loss, primarily convective, to the surroundings.
The wire is cooled by the impinging flow, and when the velocity changes also the convective heat-transfer changes, lowering the temperature of the wire and thus its resistance. This change in the resistance of the hot-wire filament is measured by an electronic device which contains a Wheatstone bridge circuit.

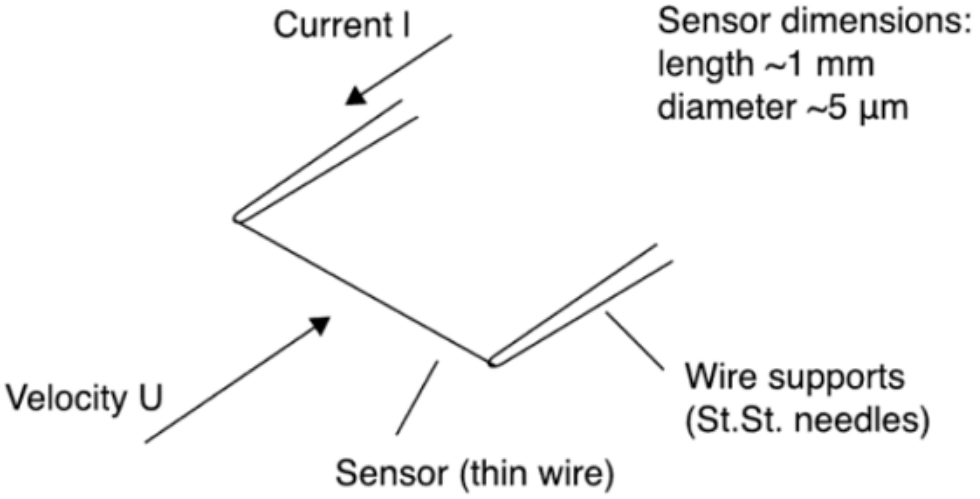

Figure 2.3: Schematic of a hot-wire anemometer,[22].

Hot-wire anemometers are well suited for turbulent flow measurements due to their extremely good spatial resolution and frequency response (unfiltered) up to 50

kHz. Furthermore, they are cheaper than other velocity measurement techniques such as laser Doppler anemometry (LDA) or particle image velocimetry (PIV).
On the other hand, they come with several disadvantages such as:

- Need for frequent calibration procedures: since are very sensitive to variations of ambient parameters such as temperature;

- Extreme fragility;

- Intrusive method: the wire must be in contact with the flow, the supports and also the wire itself alter the flow.

Governing equations

From the energy balance of the wire of the anemometer:

$$\frac{dE}{dt} = W - H \tag{2.31}$$

Where E is the thermal energy stored by the wire, W is the power provided to the wire by the Joule effect and H is the heat rate exchanged with the surroundings. At equilibrium, H is equal to W. In principle, H is the sum of the heat-exchanged through convection with the fluid, the heat conducted to the prongs and the heat radiated to the surroundings. If we assume that the radiation losses are negligible and the conduction to the prongs is small due to the design of the wire (i.e. ratio L/D large enough) the only term that remains is convection.
We can introduce the Nusselt number which expresses, in a non-dimensional form, the convective heat-transfer coefficient:

$$\mathrm{Nu} = \frac{h \cdot d_w}{k_f} \tag{2.32}$$

where k_f is the thermal conductivity of the fluid and d_w is the wire diameter. In general, the Nusselt number is a function of many parameters such as the Mach number, Prandtl number, Grashof number, Reynolds number and the overheat ratio

but if we assume that the Reynolds number is large enough to be in the forced convection regime and the flow is incompressible the Nusselt number can be expressed as:

$$\mathrm{Nu} = \mathrm{Nu}\left(\mathrm{Re}, \frac{T_w - T_a}{T_a}\right) \tag{2.33}$$

where Re is the Reynolds number and $\frac{T_w - T_a}{T_a}$ is the overheat ratio.
The wire diameter is constant and the Re_w only depends on the free-stream velocity U; therefore, it can be expressed as:

$$\mathrm{Nu} = A_1 + B_1 U^n; \tag{2.34}$$

where usually $n = 0.5$ Furthermore, by combining other equations with Equation 2.34 , the result is the so-called King law:

$$\frac{I_w^2 R_w}{R_w - R_a} = A + BU^n; \tag{2.35}$$

Finally, by expressing V_w as the product of I_w and R_w, the voltage across the hot-wire can be written as:

$$V_w^2 = A + BU^n; \tag{2.36}$$

Operating modes

The hot-wire anemometer can be operated in two different modes:

- Constant current anemometer (CCA): In this mode the current that passes through the wire is kept constant, once a specific overheat ratio has been selected, the Wheatstone bridge is kept in balance by acting on the cable resistance and an adjustable resistance. The resistance change of the sensor is measured through the output voltage of the Wheatstone bridge. The output voltage is in the order of millivolts; therefore, an amplifier is needed to have an accurate measure.

  In this mode, the frequency response is quite low (i.e. up to 1 kHz) because the thermal inertia of the wire limits it. Nowadays CCA mode is used as a

cold-wire anemometer to measure temperature fluctuations.

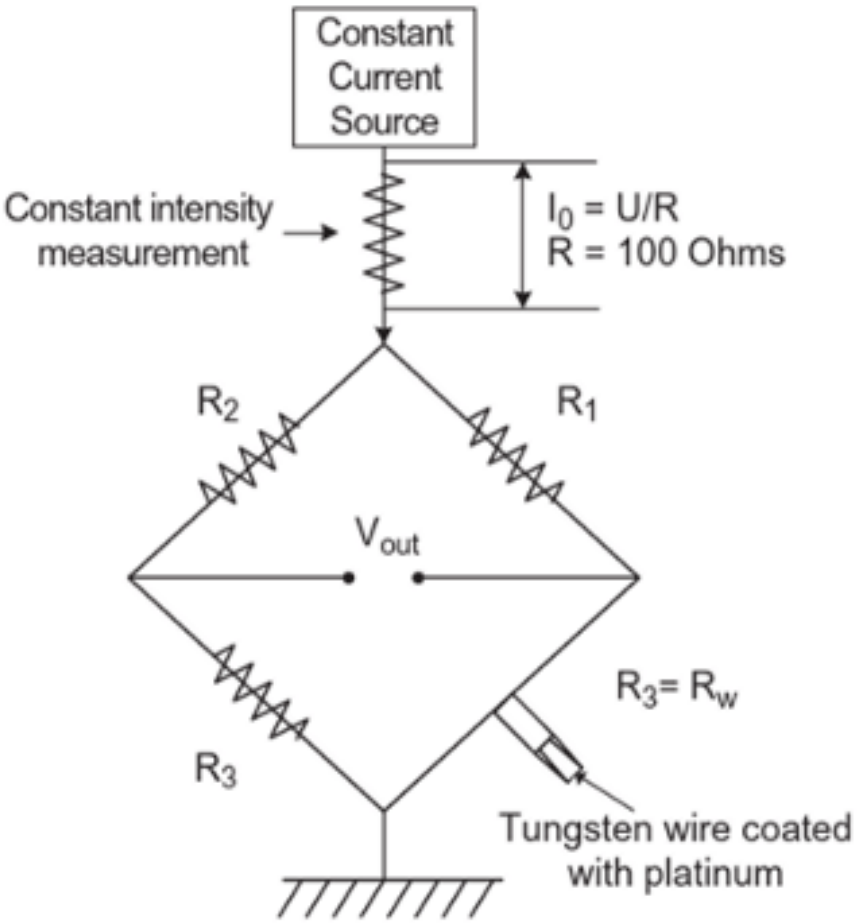

Figure 2.4: Schematic of the CCA bridge circuit,[22].

- Constant temperature anemometer (CTA): In this mode the temperature of the wire, and thus its resistance, is kept constant by a feedback loop which feeds current in the Wheatstone bridge proportionally to the velocity change, the bridge is always balanced.

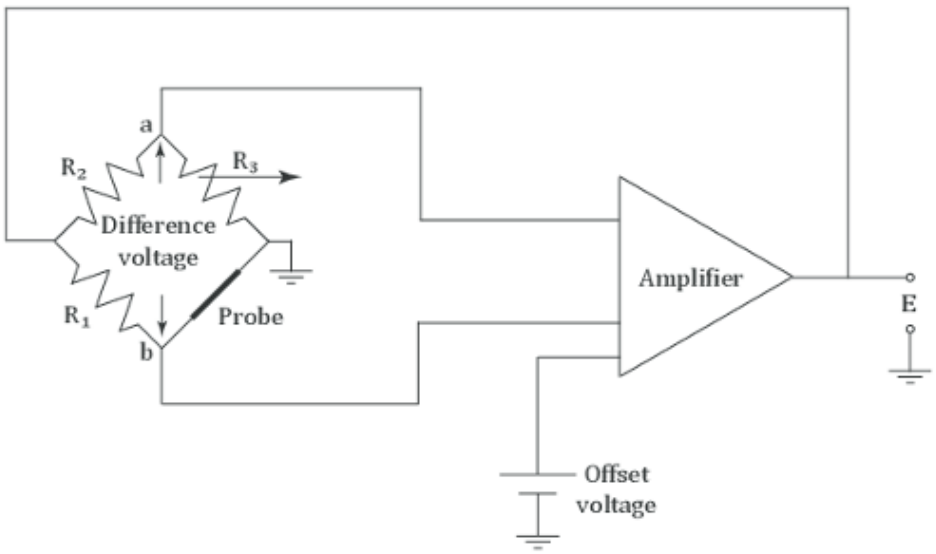

Figure 2.5: Schematic of the CTA bridge circuit, [22].

The overheat ratio is selected in advance and kept constant, this will determine the value of the variable resistance of the bridge. The goal is to keep the bridge balanced (i.e. output voltage equal to 0), we measure the amount of current needed to keep the bridge balanced. In this operational mode, the frequency response is much larger than CCA, up to 10 kHz, because is only determined by the electronics of the feedback loop. The drawback of CTA was that such a system has an unstable behaviour due to the feedback loop, but nowadays this is not an issue anymore: therefore, CTA is the operating mode universally adopted for turbulent velocity measurements.

Calibration procedure

A hot-wire anemometer's calibration procedure is used to establish the relationship between the anemometer output voltage and the velocity value. The hot-wire

is sensitive to ambient conditions and each hot-wire has a specific calibration curve that changes with ambient conditions, therefore the calibration procedure should be done before every experiment.
A Planar Air Tunnel (PAT) has been used to calibrate the hot-wire. It is a planar wind tunnel specifically developed for the calibration of hot-wire probes. The anemometer is placed at the exit of the PAT, which is operated at different velocities, the output consists of a set of voltage values that increase with velocity. Each voltage value is associated with a velocity value, which is obtained by a static Pitot tube probe.
Eventually, a calibration curve is obtained fitting these calibration points according to predetermined calibration curves, such as the King law (2.36) or a polynomial curve:

$$U = A_0 + A_1 V_w + A_2 V_w^2 + A_3 V_w^3 + A_4 V_w^4 \tag{2.37}$$

The results of this interpolation procedure are the calibration coefficients A_0, A_1, A_2, A_3, A_4, which allows to relate every voltage value measured by the hot-wire to a velocity value.

2.3 Thermodynamic background

Thermodynamics is the branch of physics that deals with the relationships between heat, work, temperature, and energy.
heat-transfer is a critical aspect of thermodynamics, and occurs with three fundamental processes: conduction, convection, and radiation. Each of these mechanisms operates under different principles and conditions, contributing uniquely to the overall process of energy transfer in systems. The basic requirement for heat-transfer is the presence of a temperature difference, the temperature difference, which is the driving force for heat-transfer.
The rate of heat-transfer per unit area is called heat flux and can be expressed as:

$$q = \frac{Q}{A} \tag{2.38}$$

Where Q is the total amount of heat-transfer and A is the surface, the units of heat fluxes are $[W/m^2]$.

2.3.1 Conduction

Conduction is one of the three primary modes of heat-transfer. It involves the transfer of thermal energy through a material without any movement of the material itself. This process occurs at the microscopic level as kinetic energy is exchanged between adjacent molecules or atoms. Conduction is described by Fourier's law:

$$q_{\text{cond}} = -k\nabla T \tag{2.39}$$

Which states that the heat flux q is proportional to the negative gradient of the temperature and the material's thermal conductivity k.
Conduction plays a significant role in solids where molecules are closely packed, which leads to efficient transfer of kinetic energy. It also occurs in fluids, although to a lesser extent, as molecular interactions are less frequent compared to solids.

2.3.2 Convection

Convection is the transfer of heat by the physical movement of fluid. Two mechanisms make up the convection heat-transfer mode. Energy is transferred by both the bulk motion of the fluid in addition to the random motion of the molecules (conduction). When there is a temperature gradient the movement of molecules facilitates the transfer of heat. The total heat-transfer is then caused by the sum of energy transmission by the molecules' random motion and by the bulk motion.
The heat flux exchanged through convection can be described as:

$$q_{\text{conv}} = h(T_s - T_\infty) \tag{2.40}$$

Where h is the convective heat-transfer coefficient, T_s is the temperature of the surface and T_∞ is the temperature of the fluid far away from the surface. Similar to

the velocity boundary layer, which is a thin region of fluid flow near the wall where the velocity of the fluid changes from zero at the wall (due to the no-slip condition) to the free-stream velocity of the fluid away from the boundary, a thermal boundary layer develops when a fluid at specific temperature flows over a surface which is at different temperature. The fluid particles a the wall will eventually reach the surface temperature of the plate, these particles then interact with those in the adjacent layers, facilitating heat-exchange and generating temperature gradients within the fluid. As one moves away from the leading edge, the effects of heat-transfer extend further into the free-stream, causing the thermal boundary layer to expand similarly to the hydrodynamic boundary layer.
The thickness of the thermal boundary layer δ_t is defined as the distance at which:

$$\frac{T - T_s}{T_\infty - T_s} = 0.99 \tag{2.41}$$

In convection, it is a common practice to non-dimensionalize the governing equations and combine the variables which group into dimensionless numbers. Therefore the heat-exchanged through convection can also be expressed using a dimensionless parameter called the Nusselt number, which is defined as the ratio of convective to conductive heat-transfer across a boundary, such as the surface of a solid immersed in a fluid, it can be expressed as:

$$Nu = (hL)/k \tag{2.42}$$

Where L is the characteristic length (such as the diameter of a pipe or the length of a plate) and k is the thermal conductivity of the considered fluid. The Nusselt number provides insight into whether convection (Nu $>$ 1) or conduction (Nu$\approx$ 1) dominates the heat-transfer process. Higher values of the Nusselt number indicate that convection is significantly more effective than conduction in transferring heat.
Convection can be classified into two modes:

- Natural (free) convection: Occurs when the fluid movement is caused by natural means, such as buoyancy forces which are related to a difference in density

connected to temperature differentials. For example, when air near a hot surface heats up, it becomes less dense and rises, while cooler air moves in to take its place.
In this case, the buoyancy forces are predominant with respect to inertial forces (i.e. $\frac{Gr}{Re^2} >> 1$) and therefore the Nusselt number is directly proportional to the Rayleigh number (Ra) number:

$$\mathrm{Nu} = f(\mathrm{Ra}) = C(\mathrm{Ra})^n \tag{2.43}$$

Where C and n are constants which are geometry and fluid dependent.
The Rayleigh number is a non-dimensional number associated with buoyancy-driven flows, and it is defined as the product between the Grashof number (Gr), which represents the balance between buoyancy forces and viscosity in a fluid and the Prandtl number (Pr), which compares momentum diffusivity to thermal diffusivity. Mathematically it is expressed as:

$$Ra = \frac{g\,\beta\,(T_s - T_\infty)\,L^3}{\nu\,\alpha} \tag{2.44}$$

Where:

- g is the gravitational acceleration;

- β is the thermal expansion coefficient;

- T_s and T_∞ are respectively the temperature of the surface and the ambient temperature;

- L is the characteristic length;

- ν is the kinematic viscosity of the fluid;

- α is the thermal diffusivity;

For example for a vertical plate in free convection regime equation 2.43 becomes [23]:

$$\mathrm{Nu} = 0.59\,\mathrm{Ra}^{0.25} \tag{2.45}$$

- Forced convection: This occurs when the fluid movement is prompted by external means, such as a fan or other mechanical devices. In this case, mixing between the upcoming flow and the thermal boundary layer occurs. The inertial forces are higher than the buoyancy forces (i.e. $\frac{Gr}{Re^2} << 1$) and therefore the Nusselt number is directly proportional to the Reynolds number:

$$\mathrm{Nu} = f(\mathrm{Re}, \mathrm{Pr}) = C\mathrm{Re}^n\,\mathrm{Pr}^m \tag{2.46}$$

For a fully-developed turbulent pipe flow, the Petukhov empirical equation [24], which was developed based on an analogy between the heat and the momentum transport describes the mean Nusselt number in a straight pipe for $\mathrm{Re} \geq 10^4$ ($10^4 \leq \mathrm{Re} \leq 10^6$, $0.1 \leq \mathrm{Pr} \leq 1000$):

$$\mathrm{Nu}_\infty = \frac{(C_f/2)\,\mathrm{Re}_D\,\mathrm{Pr}}{1.07 + 12.7\sqrt{C_f/2}\,(\mathrm{Pr}^{2/3} - 1)} \left[1 + \left(\frac{D}{L}\right)^{2/3}\right] \tag{2.47}$$

Where Re_D is the Reynolds number defined with the pipe diameter, C_f is the skin friction coefficient of the pipe and the last term of the equation with the D/L ratio represents the Hausen correction factor [25], which takes into account the increase in heat-transfer for short pipes. This correction factor is for a pipe with $D = L$ equal to 2. The correction factor decreases increasing the length of the pipe, and it approaches a value of 1 with increasing pipe length.

2.3.3 Radiation

Radiation heat-transfer is the process by which heat is transferred from one object to another through electromagnetic waves, unlike conduction and convection, radiation does not require matter to exchange heat and can occur without a physical medium.

All objects whose temperature is greater than absolute zero emit thermal radiation in all directions as electromagnetic waves, characterized by their frequency and

Parameter	Definition	Description
Nusselt number	$\mathrm{Nu} = \frac{hL}{k}$	Adimensionalized convective heat-transfer coefficient
Grashof number	$\mathrm{Gr} = \frac{g\beta(T_w - T_\infty)L^3}{\nu^2}$	Ratio between buoyancy forces and viscous forces.
Reynolds number	$\mathrm{Re} = \frac{u_\infty L}{\nu}$	Ratio between inertial forces and viscous forces.
Prandtl number	$\mathrm{Pr} = \frac{\nu}{\alpha}$	Ratio between momentum diffusivity and thermal diffusivity.

Table 2.1: Summary of relevant non-dimensional parameters in convective heat-transfer

wavelength λ $[\mu m]$. These waves range in wavelength from the longest infrared rays through the visible-light spectrum to the shortest ultraviolet rays.

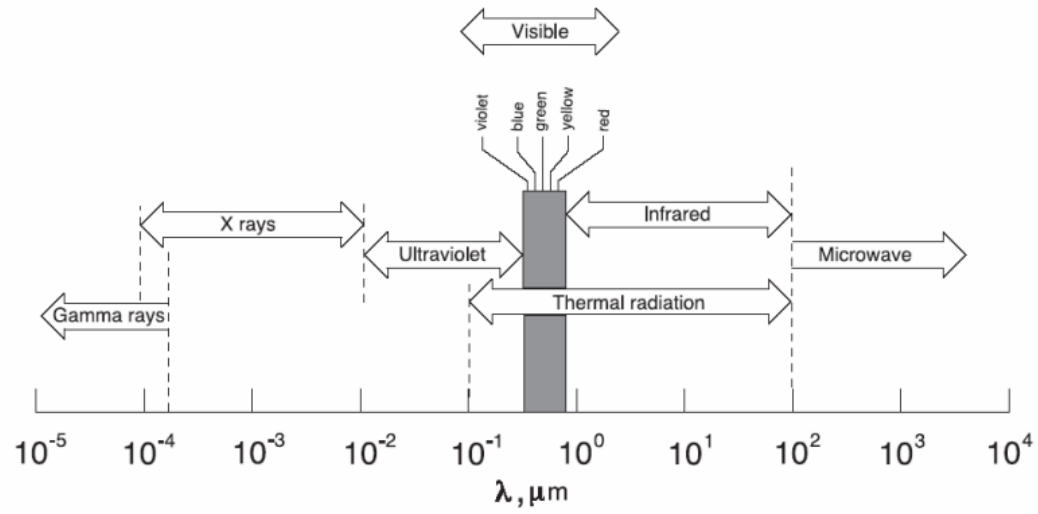

Figure 2.6: Electromagnetic spectrum,[26].

The amount of radiation emitted depends on the temperature and surface properties of the object such as the emissivity. When these waves reach another object, a portion of them is reflected, a part is absorbed, and a part is transmitted depending on the reflectivity, absorptivity, and transmissivity of the material, respectively.
The portion of the radiation reflected is called the reflectivity r, the portion absorbed is called the absorptivity a and the portion transmitted is known as the transmissivity t. These quantities are fractions of the total incident radiation, thus:

$$a + r + t = 1 \tag{2.48}$$

In the majority of solids encountered in practical applications, the transmissivity is often negligible, and therefore:

$$a + r = 1 \tag{2.49}$$

While a body that absorbs all the incident radiation is known as a blackbody, in this case, both transmissivity and reflectivity are equal to zero and the absorptivity is equal to 1.
The emissivity is a measure of a material's radiative properties, the higher it is, the higher the emission. The emissivity of a specific surface is the ratio between the thermal radiation emitted from that surface and the radiation emitted by an ideal emitter (blackbody) at the same temperature. It is expressed by a dimensionless number ranging from 0 to 1.
The emissivity of a surface depends on several factors:

- Effect of surface condition: Polished materials tend to have a lower emissivity, while materials with a high surface roughness tend to have a higher emissivity. For metallic materials also the oxidation of the surface will increase the emissivity;

- Surface coating: Applying a coating to the surface can alter its emissivity. For instance, painting or anodizing a surface can significantly increase its emissive properties;

- Material Composition: Different materials have different emissivities. Metals, for example, generally have lower emissivities compared to non-metals.

The radiative heat flux from the surface of an object to its surroundings is expressed with the Stefan-Boltzmann law:

$$q_{\text{rad}} = \varepsilon \, \sigma \, (T_s^4 - T_\infty^4) \tag{2.50}$$

Where ε is the emissivity of the surface, σ is the Stefan-Boltzmann constant $5.670 \times 10^{-8} \, \text{W/m}^2 \, \text{K}^4$ and T_s, T_∞ are respectively the temperature of the surface and the ambient temperature.

2.4 Infrared thermography (IRT)

Infrared thermography is a non-contact imaging technique for visualizing and measuring temperature variations on the surface of an object. It relies on the fact that all objects at temperatures above absolute zero emit infrared radiation, a type of electromagnetic radiation with wavelengths larger than visible light (0.4-0.7 μm range), typically in the range of 0.9 to 14 μm, and the amount of radiation increases with temperature.
Thermal cameras detect this infrared radiation and convert it into an electronic signal, which is then processed to create an infrared image.
Thermography has a wide range of applications across various fields due to its non-contact, non-invasive nature and its ability to provide real-time results. Some common applications include:

- Electrical Inspections: It is used to inspect electrical systems for hot spots caused by loose connections, overloading, damaged insulation or failing components;

- Mechanical Inspections: To monitor the condition of mechanical equipment such as motors, bearings, and pumps. Overheating components can indicate problems such as friction or lubrication issues;

-Research and Development: Thermography is widely used to study heat-transfer, thermal properties of materials, and the effectiveness of thermal management systems;

-Medical Applications: IRT is used to detect physiological changes in the human body. It can identify areas of inflammation, circulatory issues, and other anomalies.

The Infrared camera detector consists of a focal plane array (FPA) composed of pixels with a micrometer-size, constructed from various materials that are sensitive to IR wavelengths. FPA detector technologies are subdivided into two categories: thermal detectors and quantum detectors.
One of the most used thermal detectors is an uncooled microbolometer, made of a metal or semiconductor material, its working principle is the following: infrared radiation strikes the detector material that absorbs this radiation and therefore heats up, the sensor is made of a material that reacts to temperature changes with a great change of its electrical resistance. This resistance change is measured and processed into temperatures which can be used to create an image. The two most commonly used detecting materials are amorphous silicon and vanadium oxide. These kinds of sensors are cheaper and have a broader IR spectral response than quantum detectors, but they are much slower and less sensitive than quantum detectors. The latter type is generally faster and more sensitive than thermal detectors. However, they require cooling which adds complexity.
Since infrared radiation shares the same properties with visible light such as refraction, reflection and transmission the optics for thermal cameras are designed similarly to those of standard visual cameras, the difference relies on the optics material. Standard glass is a poor transmitter of IR wavelength waves, making it unsuitable for IR cameras. Therefore, IR camera lenses typically use materials like silicon (Si) and germanium (Ge) [27]. The infrared images acquired with infrared cameras are typically RGB images with an overlaying colour bar that is used to transform the RGB values into temperature readings.

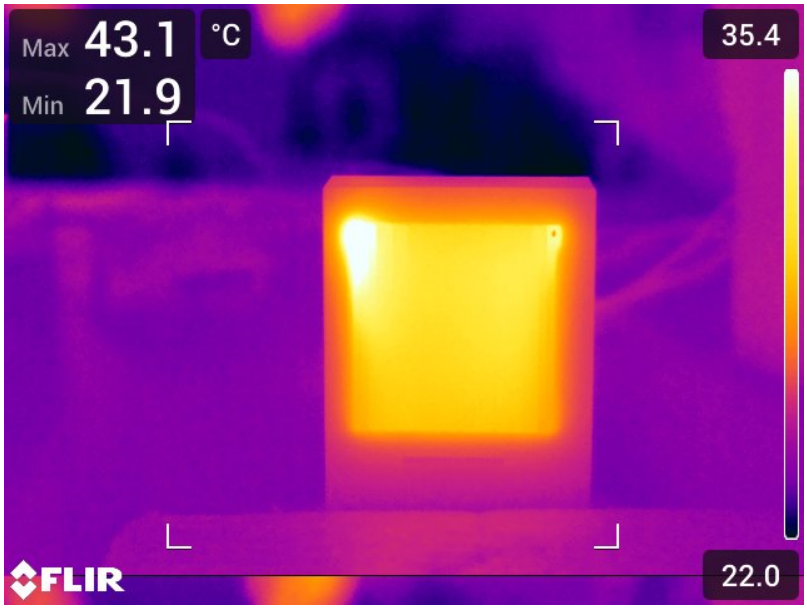

Figure 2.7: IR image of a heated painted PCB.

One crucial parameter of uncooled IR imagers is the NETD value (noise equivalent temperature difference) that describes the temperature resolution. The NETD is a measure of the thermal sensitivity of the IR camera. It represents the smallest temperature difference that a thermal imaging device can detect and is typically reported in the unit mK. The smaller it is the more performant is the infrared sensor. The most accurate uncooled IR imagers can reach NETD values of less than 60 mK.

2.4.1 Surface properties effect on IRT

The accuracy and reliability of thermographic measurements can be significantly influenced by two key surface properties:

- Emissivity: Materials with high emissivity values (i.e. close to the emissivity of a perfect emitter) emit most of their thermal energy, making them ideal for accurate temperature measurements using IRT. Conversely, materials with low

emissivity, such as metals with a polished finish like copper, emit less infrared radiation, which can lead to an erroneous temperature reading. Understanding and accounting for emissivity is crucial for interpreting thermograms accurately.

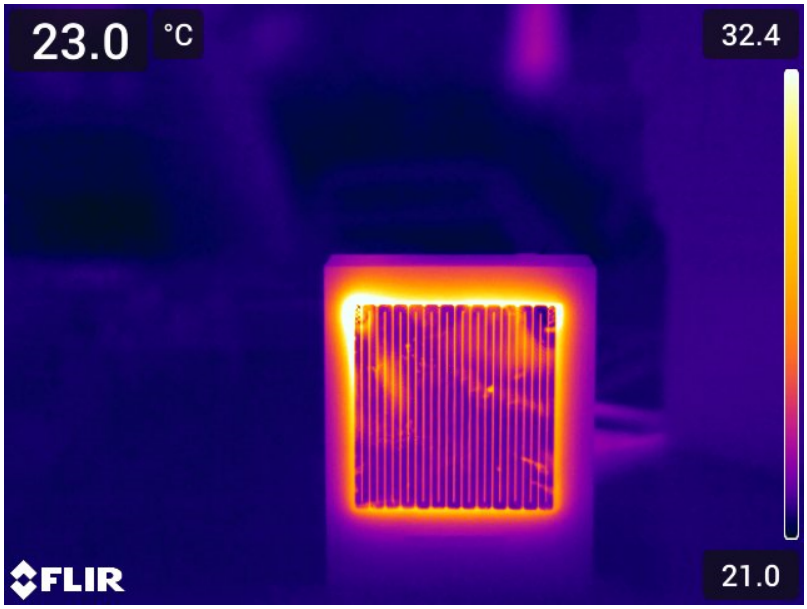

Figure 2.8: IR image of a heated PCB.

Figure 2.8 shows an infrared image of a heated printed circuit board, it is possible to notice that the polished copper tracks which are the heating elements seem to have a lower temperature than the fibreglass substrate, which is impossible, this is due to the low emissivity value of polished copper (0.03) which leads to a huge underestimation of the real temperature of the tracks.

- Reflectivity: Highly reflective surfaces can distort thermal images reflecting ambient infrared radiation or heat signatures from other sources, potentially masking the true temperature of an object. This a problem especially for metallic surfaces with a polished finish such as copper and aluminium.

Chapter 3

Experimental Facility

3.1 CICLoPE laboratory

To date, most of the experiments carried out to assess the validity of active flow control techniques aimed at increasing heat-transfer have been performed at relatively low frictional Reynolds numbers. This is especially true for the experiment of Castellanos et al [2] in which they reach a $Re_\tau = 876$. To approach as much as possible real-life applications Re_τ values, a wind tunnel that can reach higher values is needed. The CICLoPE laboratory, which stands for Centre for International Cooperation in Long Pipe Experiments, was specifically built to study high Reynolds numbers turbulent flows. The CICLoPE laboratory allows the world's best space and time-resolved measurements in turbulent pipe flows and it is the research facility that allows to reach the highest Re_τ value, ranging from about 5000 up to 47000.

3.1.1 Facility description

In turbulence studies, it is important to have a facility where the spatial size of the smallest scales l^* is large enough to be resolvable by the available measurement techniques such as hot-wire anemometry. In a pipe flow, to maintain both the Reynolds and the scales large, the physical size of the facility, in this case the diameter, should be as large as possible, for this reason, the CICLoPe wind tunnel

is a 111.5-meter tube with a 0.9-meter inner diameter. The pipe is composed of 22 five-meter-long modular elements, plus a 1.5-meter test section module at the end of the pipe. Each module is made of carbon fiber with flanges at both ends for exact element joining and is meticulously constructed to have the desired smooth surface. Additionally, each element contains four 15 cm diameter access holes, allowing for the introduction of customized parts such as potholes or measuring devices such as various traversal systems for various sensor types.

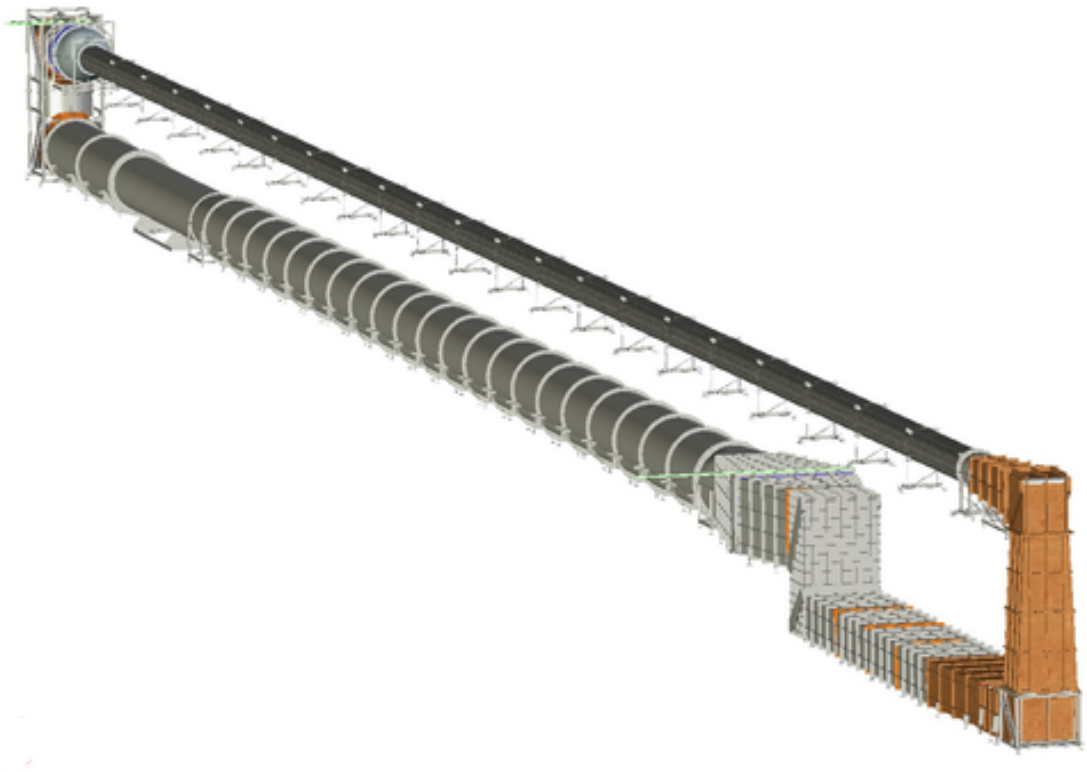

Figure 3.1: Schematic of the CICLoPE facility, [28].

The laboratory is situated inside a redeveloped underground tunnel that was part of the former Aeronautica Caproni Industries, this ensures stability of the am-

bient conditions, including temperature, humidity, and the complete absence of background noise which in turn allows for a high degree of repeatability of the experiments.

Parameter	**Value**
Total length	120 m
Pipe length	111.5 m
Test Section length	1.5 m
Inner Diameter	$0.9\ \text{m} \pm 0.1\,\text{mm}$
Inner surface roughness	$< 0.21\,\mu\text{m}$
Fan power	380 kW
Maximum speed	60 m/s
Temperature variation	$< \pm 0.1\,^{\circ}\text{C}$

Table 3.1: CICLoPE most relevant parameters.

3.1.2 Closed-loop wind tunnel

The CICLoPE Long Pipe is classified as a closed-loop wind tunnel that operates with air at ambient pressure. This closed-loop configuration enables precise control over flow characteristics, including velocity, temperature, and humidity and it is more efficient to operate compared with an open-loop wind tunnel with the same dimensions.
The closed-loop wind tunnel main sections are the following:

- Test section: It is the most important part, from a preliminary design point of view, because it can be the source of different blockage effects(e.g., Wake blockage, confinement). The design parameters are the cross-section, length and the speed range. The Long Pipe test section can be easily removed and replaced by a custom-made to meet different experimental requirements;

- Settling chamber: Inside this section screens and honeycombs (i.e., concentrated pressure drop) are placed to make the flow more homogeneous aligning

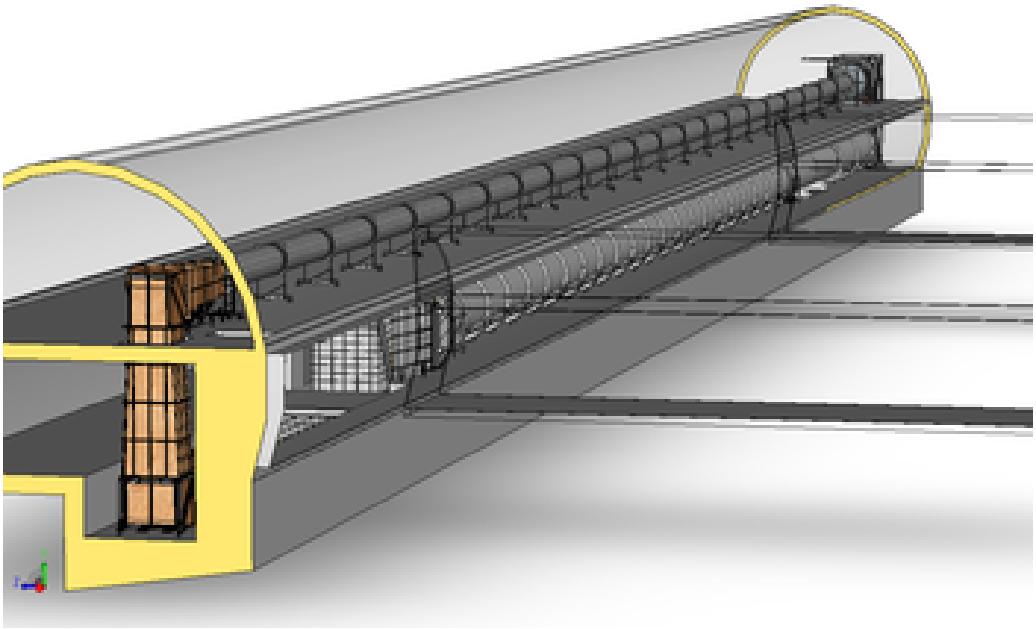

Figure 3.2: Schematic of the CICLoPE facility, [28].

it with the streamwise direction and eliminating large-scale vortices. This section is positioned in a region with low velocity (i.e., big cross-section) to minimize the losses and thus increase the overall efficiency of the wind tunnel;

- Effuser: Positioned upstream of the test section and characterized by its contraction ratio, inside this section, the flow accelerates by creating a Favourable Pressure Gradient that keeps the boundary layer attached and reduces the turbulence intensity;

- Diffuser: Positioned downstream of the test section and characterized by the opening angle, it creates an Adverse Pressure Gradient by slowing down the flow. It is used to recover as much static pressure as possible without separation of the boundary layer;

- Driving unit: To maintain the required mass-flow rate and overcome the pressure losses of the whole wind tunnel. It is positioned as far as possible from the test section because the blades could reach a high tip speed which in turn will produce a high noise level;

- heat-exchanger: It is used to maintain a stable flow temperature within the test section. It is positioned in a region of low velocity to minimize the losses.

3.1.3 Customized part

The heat-transfer measurements have to be done at the wall, and therefore a customized pothole was necessary to accommodate the PCB (e.g., test surface) and the slotted jet. The final geometry of the pothole is shown in Figure 3.3. The internal surface of the pothole was designed to fit with the internal curvature of the wind tunnel, with a curvature radius of 450 mm.

Eventually, for the final pothole assembly for the experiments inside the Long Pipe the PCB is glued to the pothole itself and the jet is fastened with two screws to the rear side of the pothole.
The actuator is a slotted jet in crossflow with a rectangular cross section of 25 mm in length and 1 mm in width, as shown in Figure 3.4. The jet's total height is 150 mm, and it is composed of three main sections:

- Final section: 10 mm in length, with a constant cross-section that matches the exit section throughout its height;

- Diffuser: provides a smooth transition from the circular cross section of the pneumatic line to the rectangular nozzle exit section. It has a total length of 125 mm;

- Cylindrical connector: This component consists of a 15 mm long cylindrical section with a constant outer diameter of 8 mm, while the inner diameter tapers from 5 mm to 4 mm along its length. This geometry enables a direct connection between the solenoid valve and the jet, or the standard pneumatic

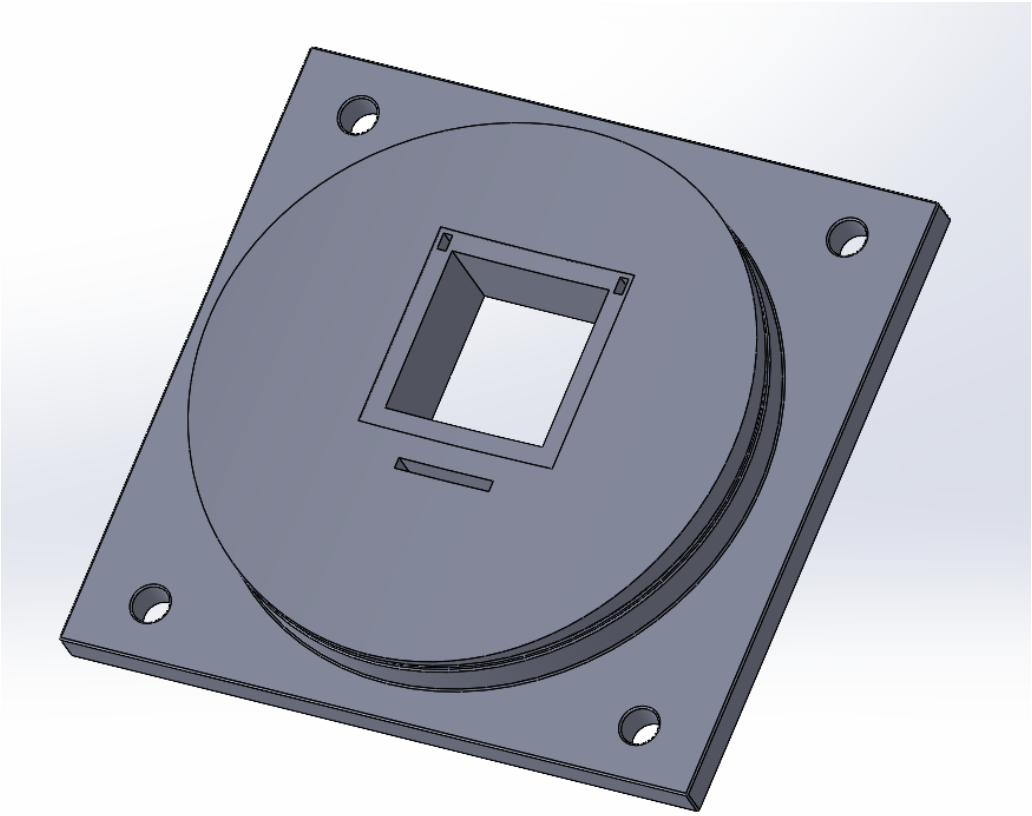

Figure 3.3: Modified pothole with cavities for the slot jet and the PCB.

tube and the jet, eliminating the need for additional cross-sectional adapters that could introduce pressure drops and therefore disrupting the flow.

The pothole and slotted jet were both produced with a Raise3D Pro2 Plus 3D printer, using PLA (PolyLactic Acid) as the filament material.

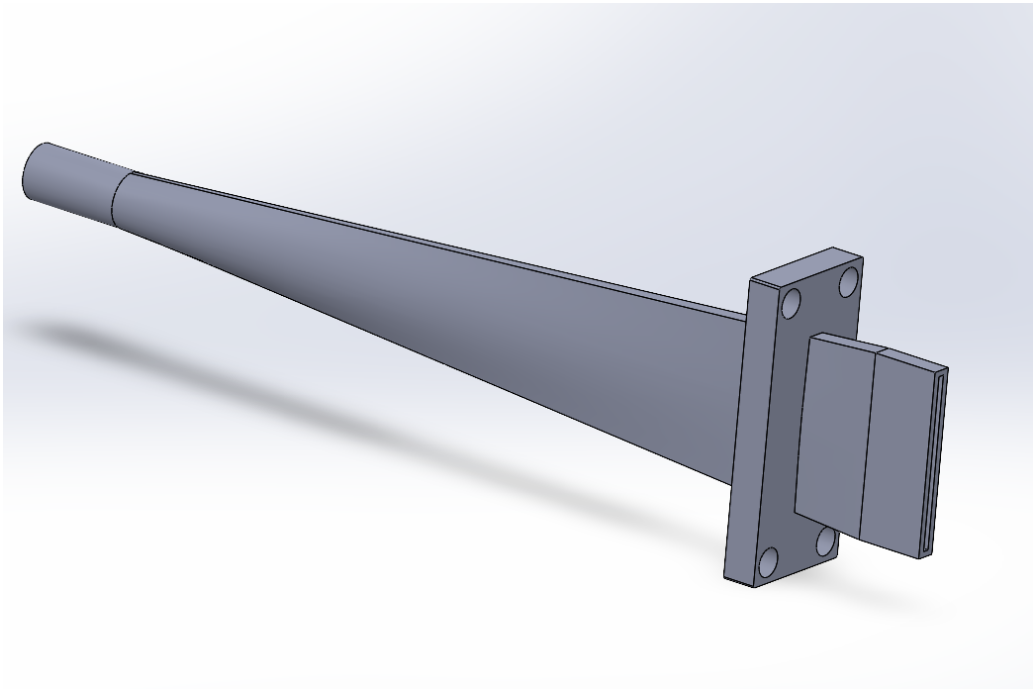

Figure 3.4: Slotted jet geometry.

Chapter 4

Experimental setup

Instrument	Model
Actuation setup instruments	
Pressure regulator	REGTRONIC IO-Link NEW DEAL
Solenoid valve	SMC SX12F-DH
Data acquisition system	NI cDAQ-9189
Power supply	Elektroautomatik PS2042B
Data Acquisition board	NI cDAQ-9189
Hot-wire CTA controller	Dantec Streamline 90N10
Printed circuit board	
Electronic circuit	
Measuring instruments	
Infrared camera	FLIR T560
Mass-flow meter	Honeywell HAFUHT0200L4AXT
Temperature sensor	PT100
Pressure transducer	MKS Baratron

Table 4.1: Actuation system and measuring instruments.

In this chapter, it is presented the instrumentation that has been used during the thesis. In table 4.1 are presented all the instruments divided into two categories: the ones used to actuate the jet, and the ones used to measure various quantities.

4.1 Actuation system

The actuation system for the pulsed-jet is composed of the following instruments: an electronic pressure regulator, a solenoid valve to provide the modulation (i.e. duty cycle and pulsation frequency) to the jet, a printed circuit board used as test surface, a power supply to power the valve and the circuit board and a circuit to generate the square wave. The pressurized air for the system is provided by the laboratory compressed-air system, which is always kept at a pressure of 9 bar.

4.1.1 Electronic pressure regulator

The pressure regulator used is a REGTRONIC IO-Link NEW DEAL, an advanced proportional precision pressure regulator designed to precisely control system pressure. This electronic pressure regulator is notable for its high precision, enabled by an electronic precision pressure sensor, and a control system that adjusts the pressure via two mini solenoid valves to reach the desired target value. It is equipped with a graphical display that shows pressure values and diagnostics. The display interface includes LEDs and buttons for easy operation. This model features quick-connect fittings that allow for easy and secure attachment and detachment of pneumatic lines, and the ports are standardized to fit common pneumatic fittings. Furthermore, the device is built to IP65 standards, which guarantees a high level of protection against dust and water ingress.

Figure 4.1: REGTRONIC IO-Link NEW DEAL,[29].

An electronic pressure regulator is required to reduce the pressure from the 9 bar supplied by the compressed air system, while simultaneously ensuring an accurate, pre-determined inlet pressure value to the valve and subsequently the jet. The inlet pressure value of the jet is directly proportional to the jet's output velocity, which in turn will determine the velocity ratio R for the experiment (see equation: 2.30).

4.1.2 Solenoid valve

The solenoid valve SMC SX12F-DH is the high-speed actuator for the square wave signal generated by the electronic circuit.A solenoid valve is an electromechanically

Fluid	air
Min inlet pressure	1 bar
Max inlet pressure	11 bar
Pressure regulation range	1.05 to 10 bar
Sensitivity	setting range 10 to 300 mbar
Accuracy	±0.3% (Full scale)
Minimum resolution	0.01 bar

Table 4.2: Electronic pressure regulator specifications.

operated valve that uses an electric current to generate a magnetic field, which in turn actuates a plunger or other mechanism against the action of a spring, when the current stops the plunger is returned to its original position by the force generated by the spring. It is a direct-acting valve which does not rely on the fluid pressure to operate. Instead, the solenoid coil's electromagnetic force directly actuates the valve. Furthermore, this specific model of the valve is equipped with a built-in filter.

Figure 4.2: SMC SX12F-DH solenoid valve,[30].

Flow rate [at 2.5 bar]	50 L/min
Min operating pressure	1.5 bar
Max operating pressure	6 bar
Opening response time [at 2.5 bar]	1.25 ms
Closing response time [at 2.5 bar]	0.4 ms
Max operating frequency	350 Hz
Power consumption	4 W

Table 4.3: Solenoid valve specifications.

The valve's opening and closing delay times are crucial, especially at higher pulsation frequencies. SMC infers that at higher frequencies both the response time and maximum operating frequencies are not guaranteed. This can significantly impact the effective duty cycle of the actuated jet, particularly at lower duty cycles and high pulsation frequencies, where the wave's up period is shorter than the opening delay time. In such cases, flow disruption may occur. This effect, and its consequences for convective heat-transfer, will be further discussed in the following chapter.

4.1.3 Data acquisition system

Data Acquisition (DAQ or DAS) refers to the process of measuring physical phenomena and recording the data for subsequent analysis. To create a perfectly synchronized control system, a board must control the solenoid valve with a square wave while simultaneously reading the mass-flow meter values in the actuation system and temperature values inside the Long Pipe. All these actions must be controlled through NI LabView, so the board must be fully compatible with the software. For these reasons, a NI cDAQ-9189 was selected. The board connects to the computer via an Ethernet port.
A c-DAQ system always consists of a controller or chassis and the modules installed in it. The CompactDAQ Ethernet chassis, known as cDAQ-9189, is designed for distributed sensor measurement systems. It controls the timing, synchronization, and data transfer between C Series I/O modules and an external host. By combining C Series I/O modules on this chassis, a mixture of analog, digital, and counter/-

timer measurements can be constructed. For widely distributed measurements, the chassis uses Time Sensitive Networking (TSN) to offer precise, synchronized timing over the network. An integrated network switch for easy daisy-chaining is built into the chassis. Additionally, the chassis includes four 32-bit general-purpose counters/-timers accessible by a hardware-timed digital C Series module for applications such as quadrature encoders, PWM, and pulse train generation.

Figure 4.3: NI cDAQ-9189,[31].

The modules are small boards that can be connected in the slots of the chassis through the serial connector. In this setup are necessary two different modules:

- NI 9263: It is compatible with LabVIEW and the NI cDAQ-9189 chassis and is the module selected to control the solenoid valve. As output, it generates an analogue wave. This signal is then acquired and analyzed as it serves as the reference signal that triggers the solenoid valve;

- NI 9215: is used for acquiring analog inputs from the hot-wire and the square wave signal generator. Specifically designed for use with NI CompactDAQ, the NI 9215 features four simultaneously sampled analog input channels and 16-bit successive approximation register (SAR) analog-to-digital converters (ADC).

Figure 4.4: NI 9263 module,[31].

Finally, the hot-wire is operated through a Dantec StreamLine 90N10 frame with 90C10 CTA modules. Since a single-wire probe was used, only one CTA module was necessary. The CTA modules include a Signal Conditioner, which matches the CTA bridge output voltage to the input range of the A/D converter board in the PC and performs signal filtering. The modules can operate in both DC and AC modes.
They feature an input Offset circuit that can subtract up to 10 Volts from the bridge output voltage with a resolution of 1 mV and a Gain function that amplifies the resulting signal up to 1024 times. The AC voltage signal from the CTA can be low-pass filtered (10 kHz) to reduce any high-frequency noise associated with the electronic circuits and cables.

Figure 4.5: StreamLine 90N10 with CTA modules 90C10.

4.1.4 Electronic Circuit for Solenoid Valve Actuation

An electronic circuit has been used to create the square wave signal to actuate the solenoid valve. The circuit components include:

- A 24 VDC power supply;
- The NI-9263 module connected to the cDAQ 9189;
- An IRFZ-44N MOSFET;
- Two resistors (1 kΩ and 10 kΩ);
- The solenoid valve.

The operation of the circuit is as follows: the cDAQ 9189, together with the NI-9263 module, generates a square wave signal ranging from 0 to 6 VDC. This signal is used to trigger the IRFZ-44N MOSFET, which operates as a switch. When combined with a constant 24 VDC signal from the power supply, the MOSFET produces a square wave signal that ranges from 0 to 24 VDC, meeting the solenoid valve's requirement for a 24 VDC input.
A MOSFET (Metal-Oxide-Semiconductor Field-Effect Transistor) is an electronic

component with three main terminals: source (S), gate (G), and drain (D). Its operation is straightforward: when the voltage between the gate and the source (V_{GS}) is below the threshold voltage (V_{TH}), the MOSFET is in the "OFF" state, acting as an open switch. Conversely, when V_{GS} exceeds V_{TH}, the MOSFET turns "ON" allowing current to flow between the drain and the source.
This setup ensures that the solenoid valve is actuated accurately, synchronized with the square wave signal generated by the NI-9263 module and controlled via the cDAQ 9189 system, all of which are managed through NI LabVIEW software.

4.1.5 Printed circuit board (PCB)

The printed circuit board (PCB) used in this thesis is modelled as a heated-thin-foil heat-exchanger.

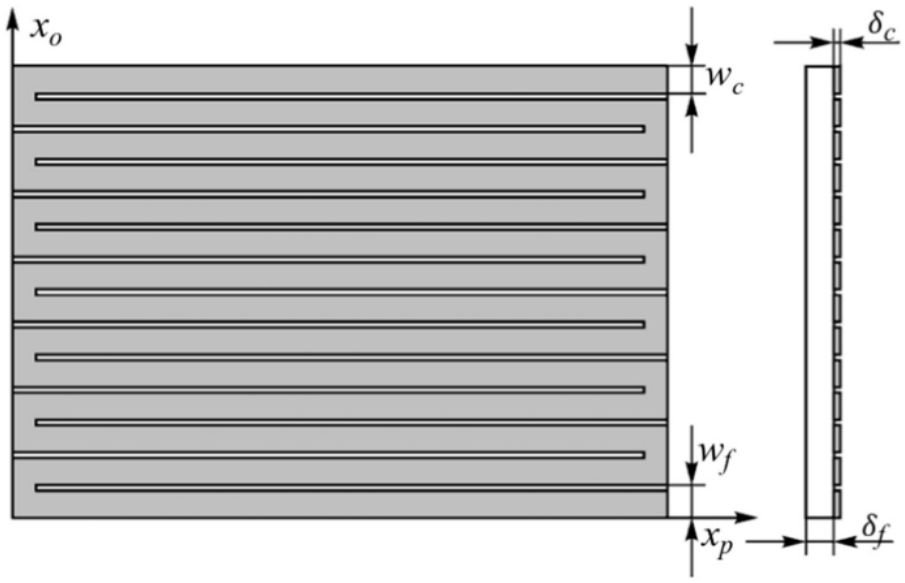

Figure 4.6: Schematic of the employed PCB,[32].

The PCB was designed to obtain a spatially-uniform distribution of the Joule heating effect and at the same time to be flexible to follow the curvature of the Long

Pipe. To achieve these characteristics the specific PCB has a constant copper track cross-section (thickness and width), a regular arrangement of the tracks, and a thin gap between them t_g. The copper rails are positioned across a fiberglass substrate, which has a thickness δ_f and a constant width w_c, pitch w_f, and thickness δ_c of the copper rails.
Thermal gradients across the thickness of the heat flux sensor can be considered negligible since the Biot number (Bi = $\frac{ht}{\lambda}$ where h is the convective heat transfer coefficient, k is the foil thermal conductivity coefficient and t is the thickness of the PCB) is small enough.

Test surface dimensions	55 × 55 mm
w_c	1.8 mm
w_f	2 mm
t_g	0.2 mm
δ_c	12 μ m
δ_f	0.5 mm
Bi	0.000014

Table 4.4: PCB specifications.

This thesis aims to assess the convective heat-transfer enhancement provided by the pulsed-jet, the PCB has been used as a heated test surface for the creation of a specific thermal gradient, specifically the reference temperature of the flow is $T_\infty = 20°\text{C}$ and we want to create a temperature difference of $\Delta T = T_w - T_\infty = 10°\text{C}$ to have an adequate heat-exchange between the flow and the PCB that can be measured accurately by the infrared camera.
The convective heat-transfer coefficient h is computed by posing a steady state energy balance, modelling the PCB as a heated thin-foil:

$$h = \frac{q_{\text{joule}} - q_{\text{rad}} - q_{\text{cond}}}{T_w - T_{aw}} \tag{4.1}$$

Where:

- q_{joule} is the heat flux provided by the Joule effect, obtained with a stabilized

power supply providing a constant voltage and current to the circuit. It is computed as:

$$q_{\text{joule}} = \frac{IV}{A} \tag{4.2}$$

- q_{rad} is the radiative heat flux to the surroundings, it is computed using equation (2.50) assuming that the environment behaves as a blackbody at a temperature equal to that of the freestream. The PCB copper tracks are made of copper which comes with a polished finish, thus they have a low emissivity value, as mentioned before this could lead to erroneous temperature measurements by the infrared camera. To overcome this issue front and rear surfaces of the PCB were painted with two layers of opaque black paint with an emissivity value of 0.95. The latter is then assumed to be the emissivity value of the PCB surfaces;

- q_{cond} is the conductive heat flux from the 4 ends of the sensor that are in contact with the pothole. The Fourier law (equation 2.39) cannot be used in this specific case because it is valid for materials with isotropic thermal conductivity, but the presence of the tracks leads to an anisotropic thermal behavior of the board. Although the copper is thin, there is a significant difference in the thermal conductivities between copper and fiberglass, which results in anisotropy in the heat-exchanger's thermal behavior. To estimate the conduction heat flux in a PCB modelled as a heated thin-foil Torre et al.[32] proposes a parameter called Tangential Conduction Degree of Importance (TCDI) which essentially is a ratio between the tangential conduction term and the convective one. For the specific PCB the value of TCDI is equal to 8% and therefore the conduction heat flux can be calculated as:

$$q_{\text{cond}} = TCDI \cdot q_{\text{conv}} = 0.08 \cdot q_{\text{conv}} \tag{4.3}$$

- T_w and T_{aw} are respectively the surface temperature of the PCB, measured with the infrared camera, and the adiabatic wall temperature.

Eventually, the convective heat-transfer coefficient is expressed in a non-dimensional form with the Nusselt number.

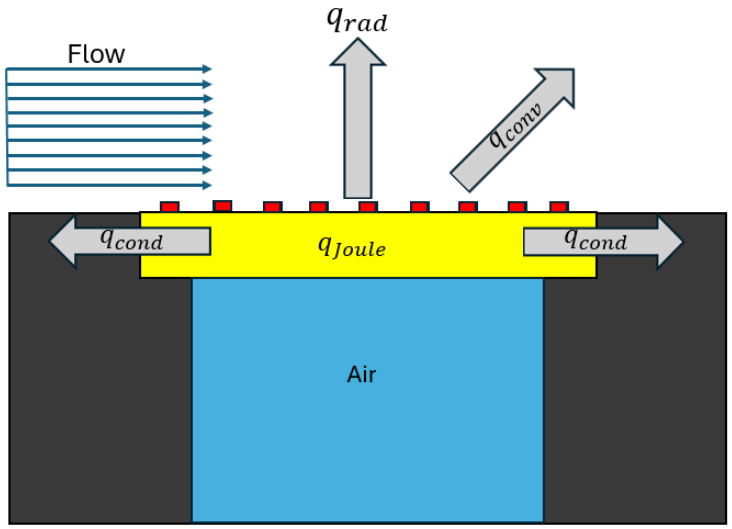

Figure 4.7: Heat-fluxes balance of the PCB.

4.2 Measuring instruments

4.2.1 Infrared camera

The infrared camera used during this thesis to measure the heat-transfer is a TELEDYNE FLIR T560, and it is a thermal detector type, in particular, the detector type is an uncooled microbolometer. The T560 is a high-resolution 640 × 480 (307200 pixel) camera equipped with built-in measurement tools and laser-assisted autofocus. FLIR thermal cameras like the T560 model include both a thermal and a visual light camera. The latter is used to enhance the thermal image resolution using an edge detector.

Figure 4.8: FLIR T560 Infrared camera,[33].

The camera detector senses the infrared radiation emitted by objects within its field of view. This radiation is then processed by the camera's built-in electronics, which translate the raw data into temperature values. This conversion allows us to visualize and measure temperature differences in real time. The initial calibration of the camera is performed by the manufacturer itself to ensure accuracy.
The camera can be triggered remotely using the FLIR research studio ®, thermal images can then be exported in many formats such as csv, tiff, etc.
The FLIR T560 thermal camera features an automatic calibration system that uses a mechanical shutter to ensure accurate and consistent temperature readings. When the thermal camera displays "calibrating" it adjusts for the deviation in response of each individual detector element (pixel). In thermography, this is called a nonuni-

formity correction (NUC). It is an offset update, and the gain remains unchanged. During the NUC, a shutter (internal flag) is placed in the optical path, and all the detector elements are exposed to the same amount of radiation originating from the shutter. Therefore, in an ideal situation, they should all give the same output signal. However, each element has its own response, so the output is not uniform. This deviation from the ideal result is calculated and used to mathematically perform an image correction, which is essentially a correction of the displayed radiation signal [33]. The NUC is usually performed during camera start-up or when the environment temperature changes.

Thermal sensitivity (NETD)	<40 mK at 30 °C
Accuracy	2% of reading
Object temperature range	-20 °C to 120°C; 0 °C to 650 °C
Spectral range	7.5 - 14 μm
Frame rate	30 Hz
Detector resolution	640 × 480 pixels
Focal length	17 mm
Field of view	24 °× 18 °
Mounted lens	24 °

Table 4.5: FLIR T560 specifications.

4.2.2 Massflow meter

The mass-flow meter used in the experimental setup is the Honeywell Zephyr HAFUHT0200L4AXT, a high-precision device known for its quick response time, high stability, and low sensitivity to thermal effects. This meter features a 12-bit resolution, ensuring accurate and detailed measurements of flow rates. Controlled by an Arduino Uno board, the HAFUHT0200L4AXT utilizes the I2C standard for digital communication, which includes a specific slave address. Upon power-up, the initial read returns the two most significant bytes of the serial number, followed by the two least significant bytes on the subsequent read. For optimal performance, it is crucial to allow the sensor to be powered for the startup time before the first

read, and to wait 10 ms for command response time before the second read. This mass-flow meter's precision and reliability are essential for accurately monitoring and controlling the flow rates in the experimental setup, ensuring the consistency and accuracy of the data collected. The integration with the Arduino Uno board facilitates easy data acquisition and processing.

Figure 4.9: Mass-flow meter,[34].

The mass-flow meter is positioned before the valve to avoid introducing pressure losses and reducing the effective duty cycle that could result from flow disruption if placed downstream. This placement allows the flow data to be used to accurately estimate the effective duty cycle by comparing the data from each test case, defined by specific frequencies and duty cycles, to the steady jet case. This method ensures precise and reliable measurements.

4.2.3 Temperature sensor

In this experiment, a PT100 temperature sensor was employed for both hot-wire calibration and continuous temperature monitoring inside the Long Pipe throughout the experimental campaign. The PT100 sensor is part of the RTD (Resistance Temperature Detector) family, which measures temperature changes by exploiting the

Full scale (FS) flow	200 SLPM
Flow response time	1 ms
Resolution	2 mm
Accuracy	0.5% FS
Operating temperature range	-20°C to 70 °C
Proof pressure	10.3 bar
Supply voltage	3 to 10 VDC
Bus standards	I2C fast mode (up to 400 kHz)

Table 4.6: Mass-flow meter specifications.

variation in electrical resistance of metals. RTD sensors like the PT100 offer several advantages, including high accuracy over a broad temperature range and excellent stability. This makes them preferable to thermocouples, which are less accurate, less stable, and prone to drifting over time. RTDs are particularly suitable for lower temperature ranges where precision and repeatability are essential. However, they must be immersed in the medium being measured to avoid stem conduction errors. A practical benefit of RTDs over thermocouples is their use of standard electrical wiring, whereas thermocouples require special compensated alloys and connectors for accurate measurement along the entire length of the instrument connection.

4.2.4 Pressure transducers

The pressure measurement circuit includes all the instruments used for hot-wire calibration and centerline velocity measurement inside the Long Pipe. This setup includes two MKS Baratron 120AD pressure transducers connected to the MKS PR4000B pressure controller. The MKS Baratron 120AD is a high-precision pressure transducer that measures absolute pressure using a capacitance manometer, providing accurate readings across a wide range of pressures. The MKS PR4000B interfaces with the Baratron transducers, supplying power, signal conditioning, and displaying pressure measurements, thereby allowing real-time monitoring and control.

Figure 4.10: PT100 temperature sensor.

Figure 4.11: MKS Baratron and MKS pressure transducer,[35].

The first pressure transducer had a pressure range of 10 Torr and was connected to the static Pitot probe, while the second transducer measured the ambient pressure with a range of 1000 Torr. The 120AD Differential combines the proven 698 Baratron High Accuracy Sensor and 270 signal conditioning electronics oscillator, de-

modulator, and amplifier within a single high impact enclosure. The compact 120AD Differential can be powered by 24-30 VDC or ±15 VDC, and provides a high-level 0-10 VDC output.

Standard features include a temperature-controlled sensor set to 45°C, remotely activated range turn-down capability to provide Full-Scale output of 0-10 Volts for 100% and 10% of the sensor range. To enhance the accuracy of the instrument, the transducers are enclosed in a 45 °C ambient environment, ensuring that temperature changes in the surroundings do not affect the pressure measurements.

Chapter 5

Results and discussion

5.1 Jet characterization

Jet characterization was conducted through a series of experiments to ensure precise control over the jet's relevant parameters: pulsation frequency, duty cycle and output velocity. Understanding and accurately controlling these parameters is crucial, as they significantly impact the convective heat-transfer downstream of the jet actuation. These experiments aimed at verify effective control over all the parameters of interest. All these parameters have been analyzed by acquiring the output velocity at the exit of the slotted jet, using a hot-wire anemometer. The signals have been subsequently post-processed with Matlab algorithms.

Jet exit section	25 × 1 mm
Duty cycles	25%, 50%, 75%
Pulsation Frequencies	From 50 to 300 Hz (with steps of 50 Hz)
Sampling time	60 s

Table 5.1: Relevant parameters for the jet characterization.

5.1.1 Spanwise velocity profile

For the output velocity analysis, the spanwise velocity profiles for different inlet pressures of the jet were acquired. A schematic of the experimental setup is shown in Figure 5.1 :

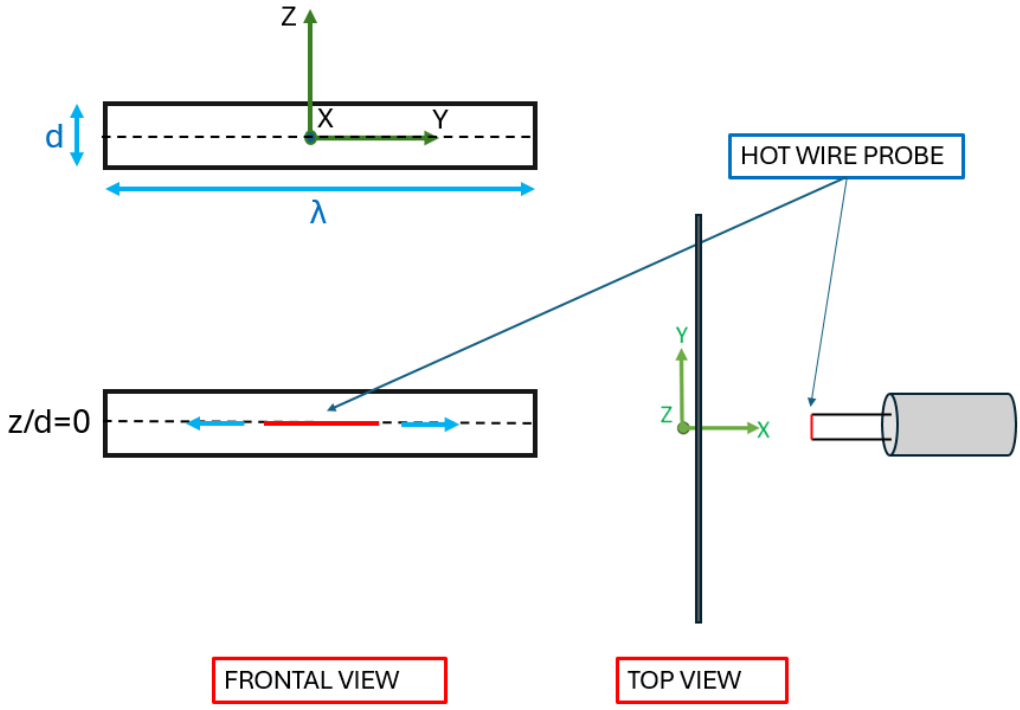

Figure 5.1: Schematic of the setup disposition for the spanwise velocity profiles acquisition.

The frame of reference is chosen with the X-axis aligned with the jet streamwise direction, the Y-axis with the jet spanwise direction, and the Z-axis with the jet chordwise direction. The origin is located at the geometric center of the jet's rectangular cross-section(i.e. where the diagonals of the rectangle intersect).

- The velocity profiles were obtained by maintaining the hot-wire probe parallel

to the spanwise direction at the chordwise location of the centerline ($z/d = 0$) and positioned at a streamwise location of $x/d = 4$;

- A total of 64 spanwise samples per profile were collected based on a pre-optimized spatial grid;
- These profiles were acquired for four different inlet pressure values: 1, 1.5, 2, and 2.5 bar;
- The movement of the probe in the spanwise direction was regulated by a stepper motor.

The results are shown in Figure 5.2.

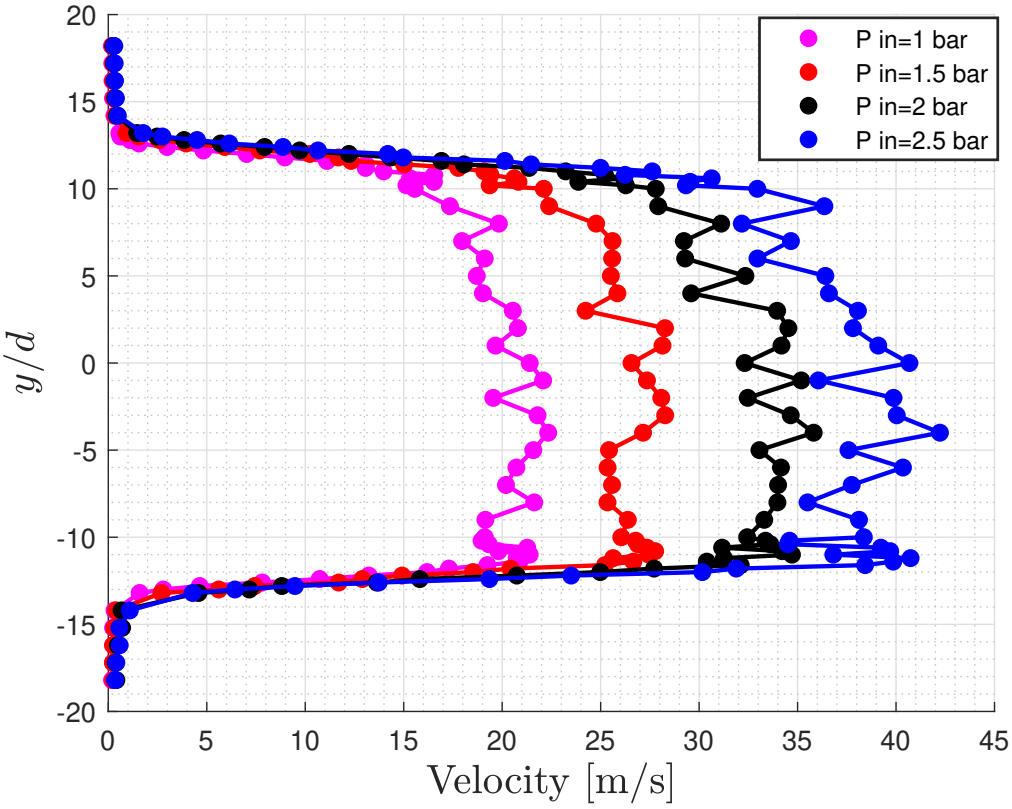

Figure 5.2: Spanwise velocity profiles at different inlet pressure values.

As expected, as the inlet pressure of the jet increases the velocity increases. Furthermore, the spanwise velocity profiles exhibit a notable uniformity and they maintain a consistent shape across all tested pressure values. However, there is a slight non-uniformity in the velocity profiles observed between the top and bottom edges, which becomes more pronounced at higher pressure values.
The spanwise velocity profiles enable the determination of the jet's mean velocity at various inlet pressure values. This mean velocity is then used to calculate the velocity ratio R between the jet and the free-stream velocity. The velocity ratio is a crucial parameter that influences the flow topology, affecting the penetration and bending of the injected flow. Consequently, these factors impact the effectiveness of the actuation system in enhancing convective heat-transfer.
For all subsequent experiments, the inlet pressure was maintained at 2 bar using the electronic pressure regulator, resulting in a jet mean velocity of 32 m/s.

5.1.2 Duty cycles analysis

The phase averaging procedure is a method used to analyze periodic signals by aligning and averaging each individual cycle. This technique helps to eliminate noise and other disturbances, making it easier to identify consistent patterns in the data. In this context, phase averaging is employed to analyze the effective duty cycle of the slotted jet. Due to the presence of noise and external disturbances, the hot-wire raw velocity signal often exhibits significant variations between individual velocity waves, which complicates the analysis of the output duty cycle. To address this, the phase averaging technique begins by identifying the indices corresponding to the high and low phases of the reference signal. A stable square wave from the data acquisition system (DAQ) is used as the reference signal, ensuring accurate identification of the signal transitions. Once the indices are determined, each velocity wave is isolated based on these points. Finally, the identified waves are averaged to produce a more consistent representation of the jet's behavior over time. The results of the phase averaging procedure are shown in Figure 5.4.

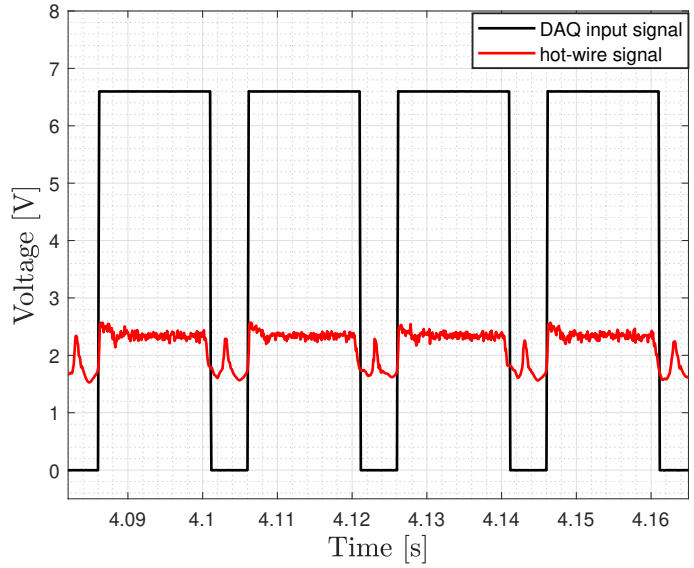

Figure 5.3: Raw voltage signals for pulsation frequency of 50 Hz and duty cycle= 75%.

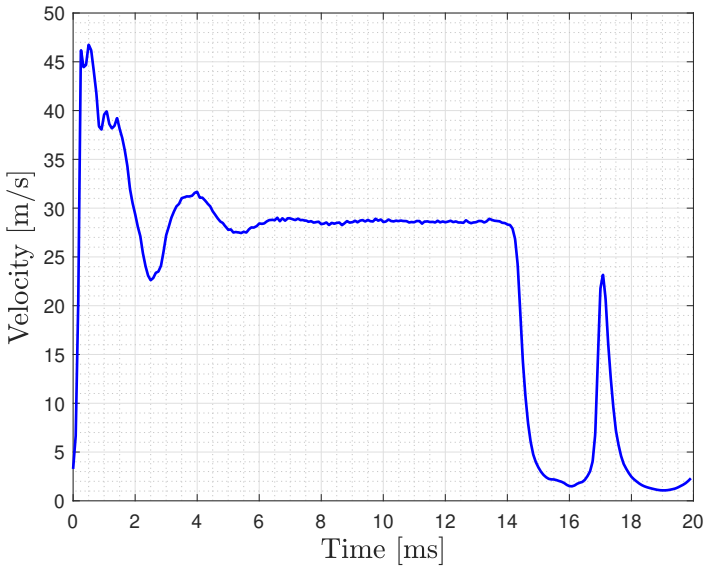

Figure 5.4: Phase-averaged outlet velocity signal for pulsation frequency of 50 Hz and duty cycle= 75%.

From the phase-averaged signal, it is possible to distinguish several features:

- Overshoot in the opening phase: During the initial phase of the opening, an overshoot is observed as the velocity does not immediately stabilize to a constant value. Instead, it exhibits a transient oscillatory behavior. This phenomenon can be attributed to the dynamics of the valve opening process, which is not instantaneous. Initially, as the valve begins to open, the flow encounters a reduced cross-sectional area, while the inlet pressure remains constant, resulting in an increased velocity;

- Opening delay time: Since the solenoid valve does not open instantaneously, it will pass a certain amount of time between the opening signal and the effective opening of the valve. For the specific valve model used this delay is certified to be of the order of 1.25 milliseconds;

- Closing delay time: This behavior mirrors that observed in the previous case, but occurs during the valve closing phase. The valve is characterized by a closing delay time of approximately 0.4 milliseconds;

- Secondary peak: This effect is not fully understood, but it is most likely a vacuum impact effect, which arises due to a rapid change in flow velocity when the valve suddenly closes. This rapid deceleration of the fluid can cause pressure waves that travel through the pipe, resulting in a shockwave that can create high-pressure spikes both upstream and downstream of the valve.

The duty cycle represents the percentage ratio of the pulse duration to the total period of the waveform. It is a crucial parameter of actuation directly linked to the volumetric flow rate injected by the jet. According to Castellanos et al., [2] adjusting the duty cycle modulates the interaction between the jet and the boundary layer. This modulation influences the formation and development of vortical structures, which are crucial for enhancing mixing and convective heat-transfer.
In this thesis, for the duty cycle estimation, an integral approach has been used,

according to Formula 5.1:

$$DC = \frac{\int_0^T u(t)\,dt}{U_{\max} \cdot T} \tag{5.1}$$

Where the duty cycle is computed as the ratio between the area under the phase-averaged signal and the area under a square wave signal with an amplitude equal to $U_{\max}$ and period T ($T = \frac{1}{f}$). As illustrated in Figure 5.4, $U_{\max}$ significantly differs from the mean value of the high part of the signal, leading to an underestimation of the duty cycle. Nonetheless, the non-instantaneous closing phase of the valve and the presence of a second peak increase the integral area, causing an overestimation of the duty cycle. It is challenging to determine which effect predominates, particularly at high pulsation frequencies. The shape of the phase-averaged signals primarily influences the calculated duty cycle values, with this effect being more pronounced at higher pulsation frequencies. According to these considerations, the duty cycle values for different pulsation frequencies are presented in the following figures:

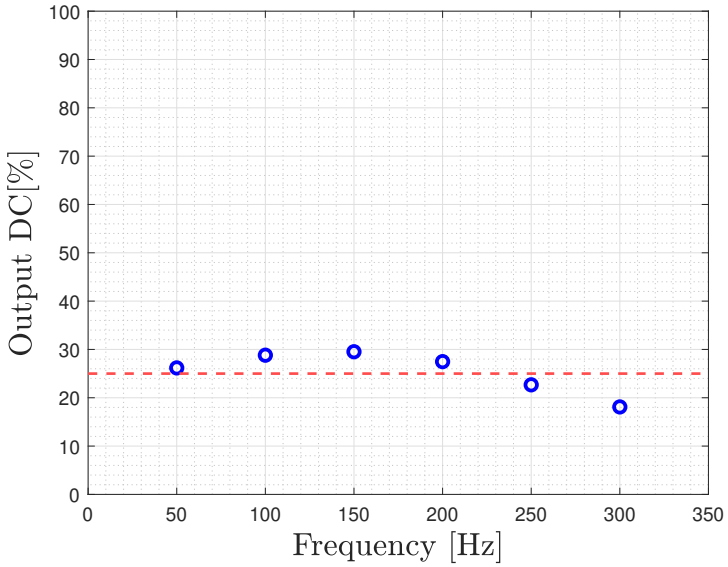

Figure 5.5: Effective duty cycle values for different input frequencies, input duty cycle= 25%.

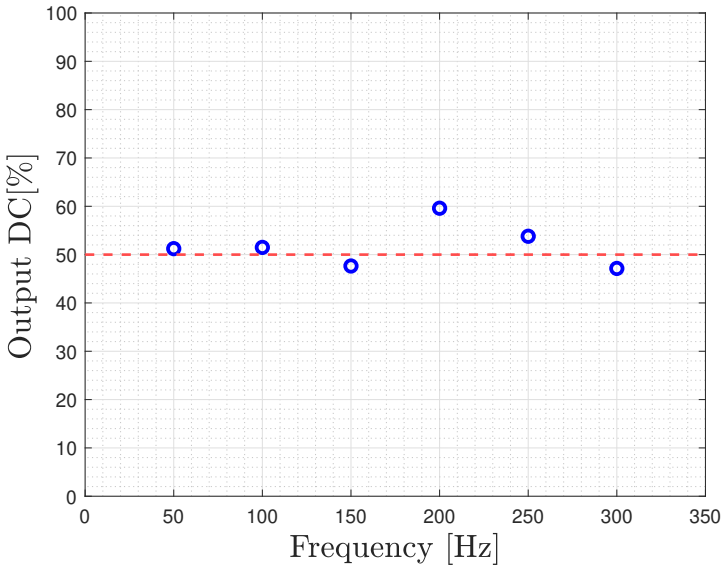

Figure 5.6: Effective duty cycle values for different input frequencies, input duty cycle= 50%.

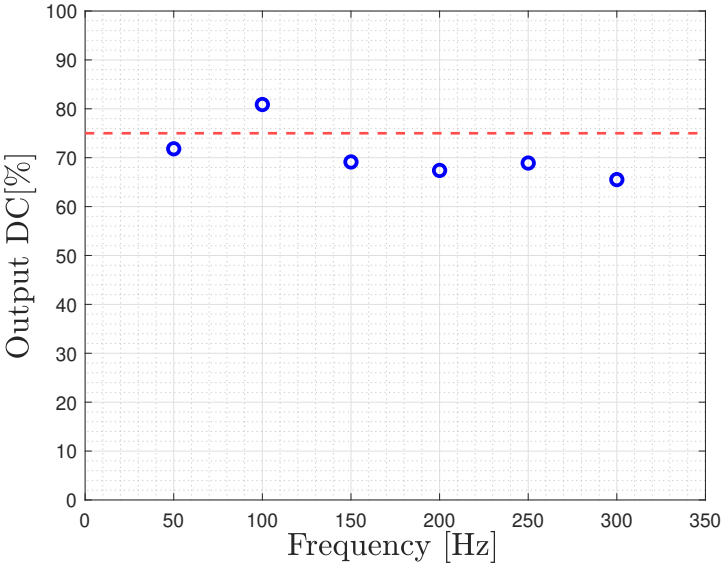

Figure 5.7: Effective duty cycle values for different input frequencies, input duty cycle= 75%.

The plots demonstrate a good agreement between the input duty cycle and the estimated duty cycle at the jet's exit section. Additionally, an important remark must be made: as the pulsation frequency increases, the period decreases significantly. When factoring in the duty cycle effect, the opening period reduces even further, as illustrated in Table 5.2:

Input frequency [Hz]	**DC=25%**	**DC=50%**	**DC=75%**
50	5 ms	10 ms	15 ms
100	2.5 ms	5 ms	7.5 ms
150	1.67 ms	3.33 ms	5 ms
200	1.25 ms	2.5 ms	3.75 ms
250	1 ms	2 ms	3 ms
300	0.82 ms	1.65 ms	2.48 ms

Table 5.2: Opening period based on input frequency and duty cycle.

It is important to consider the impact of valve delays. At higher frequencies, the phase-averaged signal increasingly diverges from the input square wave, particularly at lower duty cycles, where the valve's opening delay becomes comparable to the period of the opening itself. This effect could explain the trend seen in the plots for which at higher frequencies the measured duty cycle follows a decreasing trend.

5.2 Jet actuation effect on convective heat-transfer

The actuator employed has a rectangular shape with a length of $\lambda = 25$ mm and a width of $d = 1$ mm, injecting air into the Long Pipe at a 90°angle, and it is positioned at a distance of 3 mm from the PCB edge. The field of view (FOV) of the infrared camera comprises the entire back surface of the PCB. The frame of reference is shown in the following figures:

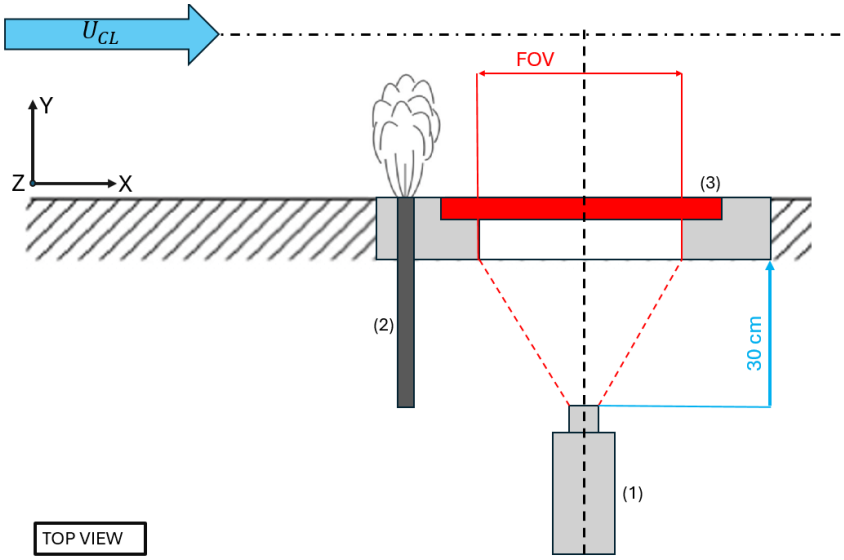

Figure 5.8: Schematic top view of the setup, (1) Infrared camera, (2) jet in cross-flow, (3) PCB.

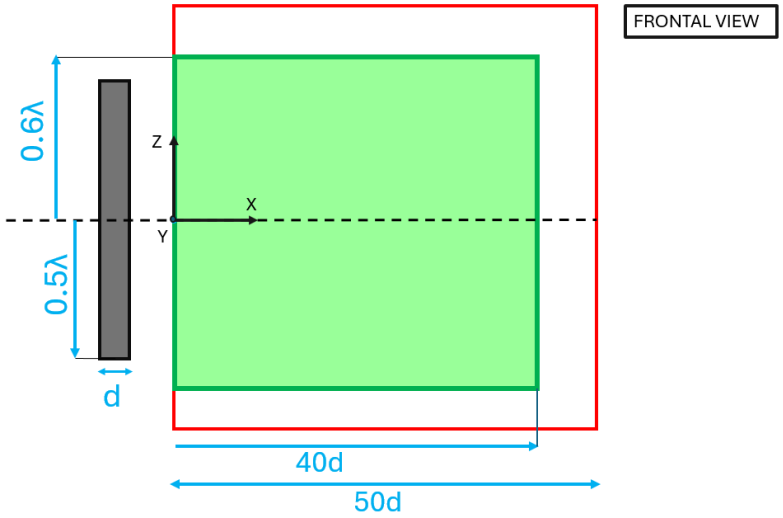

Figure 5.9: Schematic of the frontal view of the setup, red rectangle is the PCB and green rectangle is the area considered for Nu calculations.

Actuation and sampling parameters	
Jet inlet pressure	2 bar
Jet mean velocity	32 m/s
Velocity Ratio R	1
Pulsation Frequencies	From 25 to 300 Hz (with steps of 25 Hz)
Input duty cycles	25%, 50%, 75%
Sampling rate	30 Hz
Sampling time	35 s
q_{Joule}	1960 W/m^2
CICLoPE parameters	
CICLoPE centerline velocity	32.5 m/s
Re_τ	31457
Active temperature control	ON
Centerline flow temperature T_∞	20.8 °C
Ambient pressure	100.93 kPa
k_{air}	0.0265 W/mK

Table 5.3: Summary of the experimental campaign and Long Pipe parameters during the experiment.

Then thermography measurements are performed downstream of the actuation on a region comprising $1.5\lambda \times 50d$. The input power to the PCB was set to maintain a temperature difference of approximately 10 °C between the flow temperature (T_∞) and the wall temperature and was kept constant throughout the experiment. Temperature measurements of the heated-thin-foil sensor are acquired with the infrared camera at a frame rate of 30 Hz, for each acquisition 1050 frames were acquired. From these frames, the wall temperature distribution over the PCB is obtained, and from the temperature map, a distribution of the convective heat-transfer coefficient is calculated posing a steady state energy balance (see equation: 4.1). This distribution was subsequently non-dimensionalized using the Nusselt number, where the diameter of the Long Pipe was used as the characteristic length. Additionally, the adiabatic wall temperature needed to compute equation (4.1) was computed from a set of 1050 images acquired with no heating applied to the PCB while the Long Pipe was operating.

Furthermore, during valve activation, it was observed that the valve itself heats up, and therefore it could act as a heating source altering the temperature of the injected air. To quantify the influence of this effect, the temperature of the jet was measured across all duty cycles and frequencies. The results are shown in the following figure:

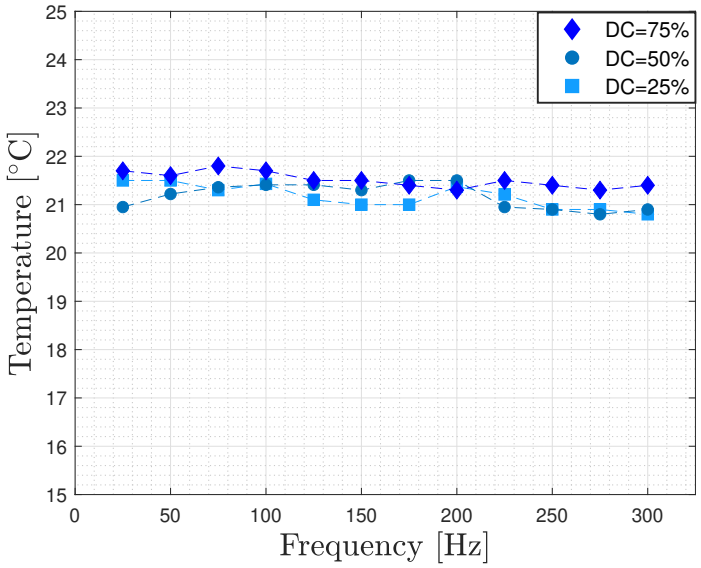

Figure 5.10: Injected flow temperature at different pulsation frequencies and duty cycles.

Figure 5.10 reveals that the jet temperature remains approximately constant, without a clear trend related to pulsation frequency. The standard deviations for each duty cycle across all frequencies were calculated ($\sigma_{\mathrm{DC25}} = 0.21°C$, $\sigma_{\mathrm{DC50}} = 0.23°C$, and $\sigma_{\mathrm{DC75}} = 0.18°C$). Given the absence of a clear relationship between frequency and jet temperature, these standard deviations were used as the temperature uncertainty applied to the wall temperature for the respective duty cycles. Consequently, in the following discussion, the Nusselt number values for different frequencies will be presented within a range to account for this uncertainty.

The Nusselt number distribution is characterized in terms of two reference conditions:

- Non-actuated jet: Wall temperature distribution acquired with heating to the PCB activated and the valve was not actuated. This case is denoted by the subscript 0;
- Steady jet actuation: Wall temperature distribution acquired with heating to the PCB activated and the jet was running continuously without pulsation. This case is denoted by the subscript sj.

The Nusselt number spatial distributions for both cases are shown in Figure 5.11 and Figure 5.12. The Nusselt number distribution for the non-actuated case agrees with the literature describing a progressive decay, while for the steady jet actuation, the Nusselt number distribution exhibits a quasi-symmetric pattern with a strong convective heat-transfer enhancement in the vicinity of the air injection. The effect of the jet is persistent even $40d$ downstream of the actuator, on the contrary; in the spanwise direction the enhancement is very localized, mainly affecting the area downstream of the jet.

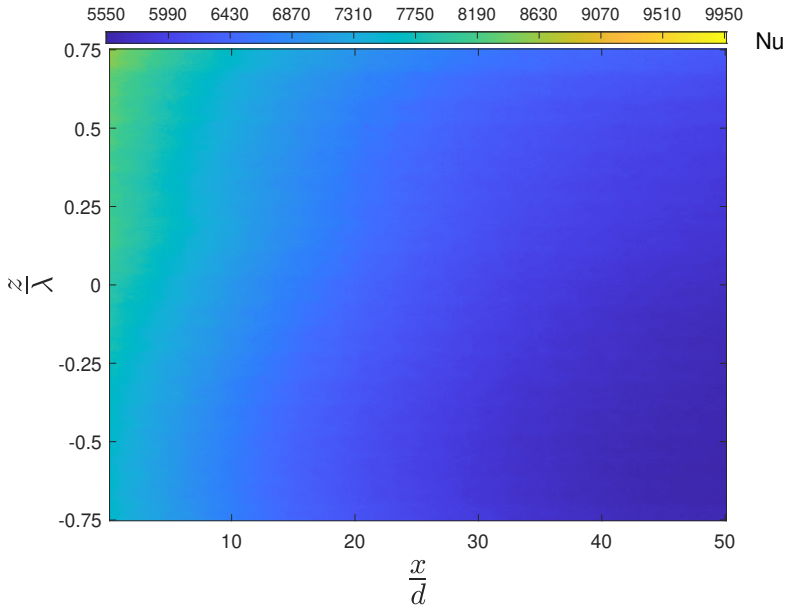

Figure 5.11: Nusselt number distributions downstream the jet for the non-actuated case.

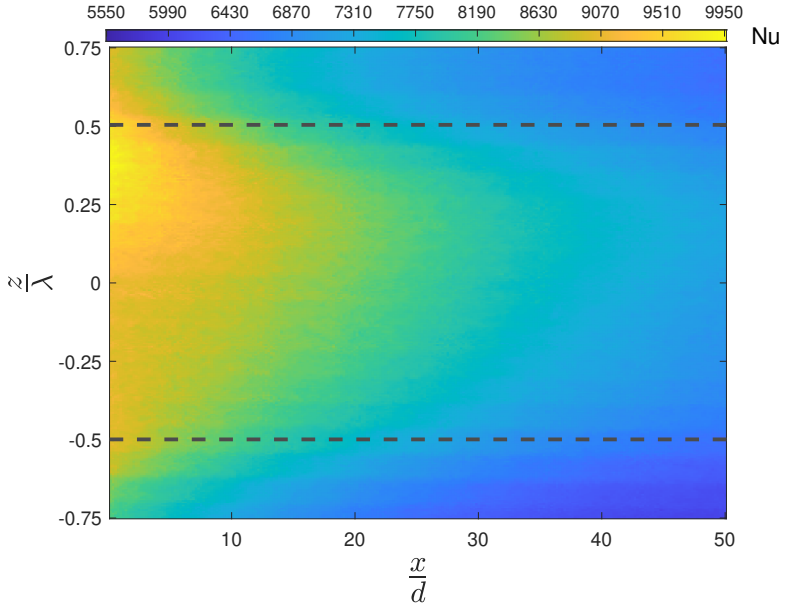

Figure 5.12: Nusselt number distributions downstream the jet for the steady jet actuation. The boundaries of the jet are highlighted with the black dashed line.

Consequently, to assess the convective heat-transfer enhancement the Nusselt number distribution is spatially averaged with an integral approach. Nusselt number was computed in the region comprised in $0 \leq x \leq 40$ and $-0.6\lambda \leq z \leq 0.6\lambda$:

$$\overline{Nu} = \frac{1}{\lambda d} \int_{-0.6\lambda}^{0.6\lambda} \int_{0}^{40d} Nu(x, z)\, dx\, dz \tag{5.2}$$

The averaged Nusselt numbers for both the steady jet and non-actuated cases were calculated. To quantify the enhancement in convective heat-transfer resulting from jet actuation, a parameter called relative enhancement is introduced. This parameter compares the Nusselt number of the actuated jet to that of the non-actuated case and is defined as follows:

$$E = \frac{\overline{\mathrm{Nu}}_{sj}}{\overline{\mathrm{Nu}}_{0}} - 1 \tag{5.3}$$

A summary of these quantities is provided in the Table 5.4

$\overline{\mathbf{Nu}}_{sj}$	$\overline{\mathbf{Nu}}_{0}$	**E**
8060	6450	0.25

Table 5.4: Summary of reference Nusselt numbers and relative enhancement.

The spatially averaged Nusselt numbers for all the actuation frequencies and duty cycles presented in Table 5.3 were computed considering the same area described before. The results are shown in Figure 5.14:

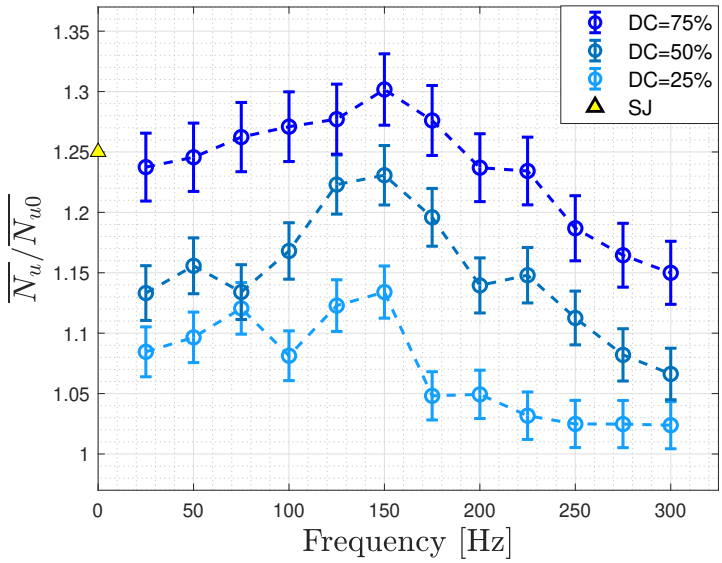

Figure 5.13: Averaged Nusselt numbers downstream of the jet normalized with the non-actuated jet case.

From the experiment results it is possible to notice the effect on the heat-transfer of both frequency and duty cycle:

- Duty cycle effect: The duty cycle has a direct effect on the convective heat-transfer enhancement since it is directly related to the amount of air injected, and thus the momentum added to the system. The data shows that an increase in the duty cycle (DC) results in a linear rise in heat-transfer. However, at higher frequencies (f $>$ 150 Hz), the Nusselt number begins to decline for all duty cycles. This decrease can be attributed to valve delays, which become predominant relative to the opening period as frequency increases, effectively reducing the actual duty cycle and consequently the amount of air injected. This phenomenon is particularly evident at lower duty cycles. As shown in Table 5.2, for DC = 25% and frequencies exceeding 200 Hz, the theoretical open time is shorter than the valve's opening delay, leading to significant flow disruption and a reduced effective injection;

- Frequency effect: The frequency effect on convective heat-transfer shows a consistent trend across all duty cycles. Initially, the heat-transfer increases, reaches a peak, and then rapidly decreases. This behavior indicates that the Nusselt number does not exhibit a linear dependency on the actuation frequency. For a given duty cycle, experimental results suggest the existence of an optimal actuation frequency, which maximizes the Nusselt number, observed at f = 150 Hz. The highest absolute performance is achieved with a duty cycle of 75% at this frequency, resulting in a Nusselt number even higher than that of the steady jet case, despite a lower amount of air being injected (as the duty cycle is directly related to the air volume injected).
  The sharp decline in the Nusselt number at higher frequencies is likely due to the above-mentioned valve delays, which become increasingly significant as the frequency increases, causing the period to decrease. This effect exacerbates the reduction in the effective duty cycle and, consequently, the amount of air injected.

5.3 Velocity ratio influence on convective heat-transfer

Literature indicates that the velocity ratio (R) significantly influences the flow topology of jets in crossflow, consequently affecting their heat-transfer performance. Additional experimental campaigns were conducted to evaluate the impact of the velocity ratio on the effectiveness of the actuation system in enhancing convective heat-transfer. These experiments maintained a constant jet inlet pressure of 2 bar, ensuring a fixed jet mean velocity. Adjusting the flow velocity also alters the turbulent Reynolds number Re_τ, enabling analysis of its impact on performance.

$\mathbf{U_{jet}}$ [m/s]	$\mathbf{U_{cl}}$ [m/s]	$\mathbf{Re_\tau}$	R
32	32.5	31457	1
32	37.6	37271	0.85
32	43.7	40247	0.7

Table 5.5: Summary of the experimental parameters.

For all the velocity ratios tested the Nusselt number distributions for the two reference cases(i.e. steady jet and non-actuated jet) and for all the pulsation frequencies and duty cycles were obtained with the same procedure described in the previous chapter. Then the spatially averaged Nusselt number was computed using the same area for consistency and then they were normalized with the reference value of the non-actuated case. The results are shown in the following figures:

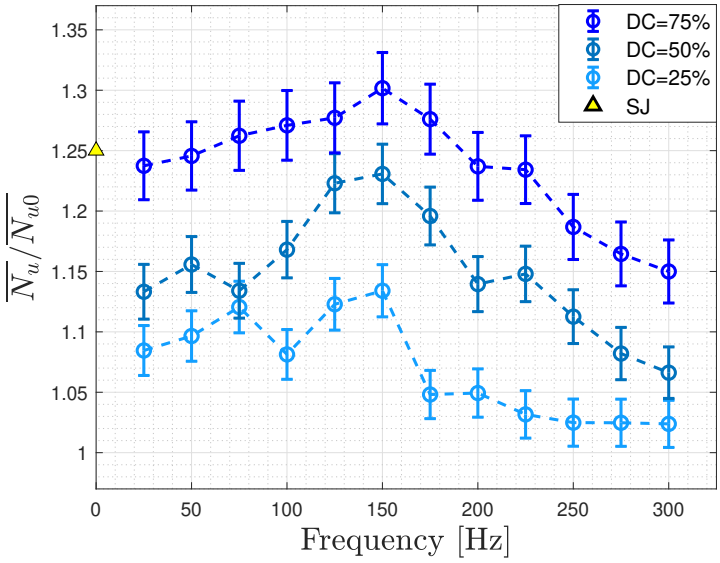

Figure 5.14: Averaged Nusselt numbers downstream of the jet normalized with the non-actuated jet case, velocity ratio $R = 1$.

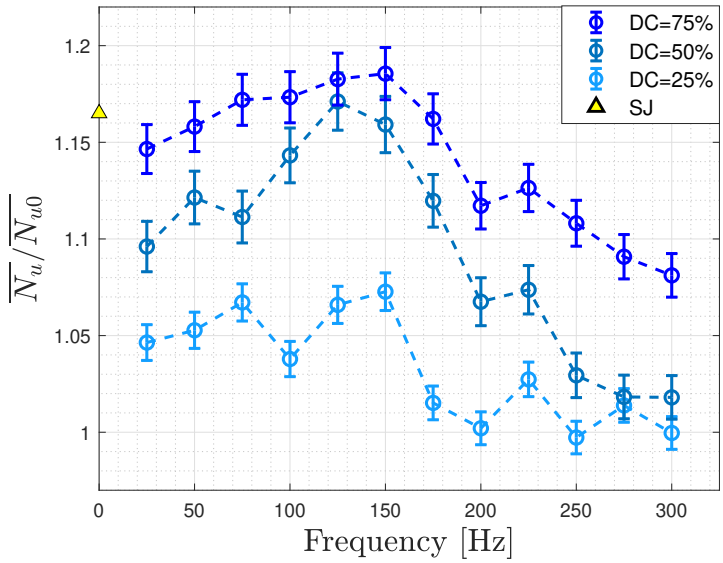

Figure 5.15: Averaged Nusselt numbers downstream of the jet normalized with the non-actuated jet case, velocity ratio $R = 0.85$.

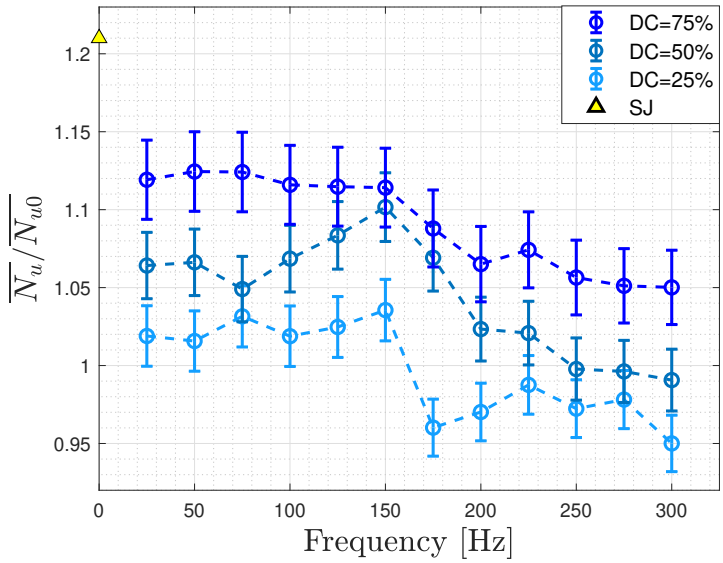

Figure 5.16: Averaged Nusselt numbers downstream of the jet normalized with the non-actuated jet case, velocity ratio $R = 0.7$.

The experimental results shown in Figures 5.14, 5.15 and 5.16 exhibit several interesting behaviours. Firstly, the linear relationship between the duty cycle (DC) and the Nusselt number is consistently confirmed across all acquisitions, which aligns with expectations since the DC is directly proportional to the amount of air injected. This correlation demonstrates that increasing the DC effectively enhances the convective heat-transfer.

Furthermore, the previously observed trend of the Nusselt number as a function of frequency is confirmed. For all tested velocity ratios, the Nusselt number increases with frequency, reaching a peak at 150 Hz before rapidly declining. However, at lower velocity ratios, this trend flattens, and the peak becomes less pronounced. This sharp decrease at higher frequencies is likely due to valve delays, which become more significant as the frequency increases.

Moreover, for a given frequency and DC value, the results reveal a progressive decay in the absolute value of the normalized Nusselt number as the velocity ratio decreases. This indicates that the convective heat-transfer enhancement from the jet becomes less significant compared to the heat-transfer of the turbulent flow itself. This effect could be due to the reduced penetration of the jet or the increased heat-transfer of the undisturbed flow resulting from the higher Reynolds number.

In summary, these observations highlight the intricate dependencies of convective heat-transfer on both the duty cycle and frequency, as well as the critical role of velocity ratio in determining the effectiveness of jet actuation in enhancing heat-transfer.

Chapter 6

Conclusions and future works

6.1 Conclusions

The objective of this thesis is to evaluate the effectiveness of an active flow control method, specifically a pulsed slot jet perpendicular to the crossflow, on enhancing convective heat-transfer. The actuation system used in this study comprises an electric circuit driving a solenoid valve and a diffuser, which creates the impinging jet. This diffuser was embedded in a customized pothole for installation in the Long Pipe facility at the CICLoPE laboratory. Additionally, a printed circuit board, modelled as a heated-thin sensor for the heat fluxes measurement, was positioned immediately downstream of the jet.

Experimental investigations were conducted to control the convective heat-transfer in a turbulent pipe flow using the pulsed-jet in crossflow. A parametric study was performed by varying the pulsation frequency and duty cycle. The characterization of the jet was achieved using a hot-wire anemometer, which provided spanwise velocity profiles for different inlet pressure values. The effective duty cycles were estimated with an integral approach, demonstrating good agreement between the input duty cycle from the DAQ and the output duty cycle measured with the hot-wire anemometer. It was observed that the duty cycles decreased at higher frequencies, likely due to the valve delays in opening and closing.

heat-transfer measurements were conducted by acquiring the heat fluxes at the wall using infrared thermography. The convective heat-transfer, expressed in a non-dimensional form with the Nusselt number (Nu), was computed for various actuation frequencies, duty cycles and different velocity ratios. The results showed a linear trend between Nu and the duty cycle, which was expected since the duty cycle is directly related to the amount of air and, consequently, the momentum injected into the system. This trend has been observed also in the work done by Castellanos et al.[2]
Furthermore, the Nusselt number demonstrated a non-linear relationship with frequency. Specifically, heat-transfer increased until reaching a peak before rapidly declining at higher frequencies. This sharp decrease is likely attributed to valve delays, which become more significant at elevated frequencies, thereby reducing the effective duty cycles. The best absolute performance of the pulsed-jet was consistently observed at a frequency of 150 Hz and a duty cycle of 75%.
It is worth remarking on an unexpected behaviour: at low Reynolds numbers none of the actuation cases performed better than the steady jet[2]. On the contrary, the experimental results at high Reynolds numbers exhibit cases with a higher efficiency than the steady jet one. This aspect is promising and should be further investigated.

6.2 Future works

6.2.1 Cold-wire measurements

During energization, the valve heats up, particularly at higher duty cycles requiring prolonged energization periods. In this experiment, the jet exit temperature was measured using a PT100 temperature sensor, but this was done outside the CICLoPE wind tunnel, separate from the main experiments. A more precise sensor should be utilized to evaluate the jet temperature's impact on convective heat-transfer accurately. Implementing a cold wire (i.e., a hot-wire anemometer operated in the constant current anemometer CCA mode) in the setup could provide rapid real-time temperature measurements and therefore more accurate estimations of the jet inlet

temperature effects on the effectiveness of the system.

6.2.2 Improvement of the setup

The current study found that the Nusselt number shows a linear increase with the duty cycle, directly proportional to the amount of air and momentum injected into the system. The frequency effect exhibited a non-linear trend, with the Nusselt number increasing until it peaked at 150 Hz, followed by a rapid decrease likely due to valve delays at higher frequencies. The next step involves implementing a more performant solenoid valve capable of operating at higher frequencies with reduced opening and closing delays. The current valve tends to decrease the effective duty cycles at higher frequencies since the delay times become comparable to the wave period. Repeating the experiments with the new valve will help assess its impact and verify if the previously observed frequency trend, with a peak at 150 Hz followed by a sharp decline, persists. Additionally, it will determine if the peak remains at the same frequency.

Furthermore, incorporating a germanium window would allow infrared thermography measurements on the front surface of the PCB, which is directly exposed to the flow. This improvement could provide more accurate temperature data, enhancing the overall understanding of the convective heat-transfer mechanisms.

Bibliography

[1] GA Romakhova. "Influence of the Cooling Technology on the Efficiency of Gas-Turbine Power Plants". In: *Power Technology and Engineering* (2022).

[2] Rodrigo Castellanos et al. "Heat transfer enhancement in turbulent boundary layers with a pulsed slot jet in crossflow". In: (2023).

[3] https://www.cfdsupport.com.

[4] K Kataoka et al. "The effect of surface renewal due to largescale eddies on jet impingement heat transfer". In: *International Journal of Heat and Mass Transfer* (1987).

[5] Yasuhiro Kamotani and Isaac Greber. "Experiments on a turbulent jet in a cross flow". In: *AIAA journal* (1972).

[6] TF Fric and A Roshko. "Vortical structure in the wake of a transverse jet". In: *Journal of Fluid Mechanics* (1994).

[7] Richard Malcolm Kelso, TT Lim, and AE Perry. "An experimental study of round jets in cross-flow". In: *Journal of fluid mechanics* (1996).

[8] SH Smith and MG Mungal. "Mixing, structure and scaling of the jet in cross-flow". In: *Journal of fluid mechanics* (1998).

[9] Luca Cortelezzi and Ann R Karagozian. "On the formation of the counter-rotating vortex pair in transverse jets". In: *Journal of Fluid Mechanics* (2001).

[10] JE Broadwell and RE Breidenthal. "Structure and mixing of a transverse jet in incompressible flow". In: *Journal of Fluid Mechanics* (1984).

[11] David S Liscinsky, B True, and JD Holdeman. "Crossflow mixing of noncircular jets". In: *Journal of propulsion and power* (1996).

[12] MW Plesniak and DM Cusano. "Scalar mixing in a confined rectangular jet in crossflow". In: *Journal of Fluid Mechanics* (2005).

[13] Axel Coussement, Olivier Gicquel, and Gerard Degrez. "Large Eddy Simulation of Pulsed Jet in Cross-flow". In: *Journal of Fluid Mechanics* (2012).

[14] Jannis Andreopoulos and Wolfgang Rodi. "Experimental investigation of jets in a crossflow". In: *Journal of fluid Mechanics* (1984).

[15] EC Mladin and DA Zumbrunnen. "Local convective heat transfer to submerged pulsating jets". In: *International Journal of Heat and Mass Transfer* (1997).

[16] Tianshu Liu and JP Sullivan. "Heat transfer and flow structures in an excited circular impinging jet". In: *International Journal of Heat and Mass Transfer* (1996).

[17] LFA Azevedo, BW Webb, and M Queiroz. "Pulsed air jet impingement heat transfer". In: *Experimental Thermal and Fluid Science* (1994).

[18] Adnan Eroglu and Robert E Breidenthal. "Structure, penetration, and mixing of pulsed jets in crossflow". In: *AIAA journal* (2001).

[19] Stephen Robert Shapiro et al. "Optimization of controlled jets in crossflow". In: *AIAA journal* (2006).

[20] RT Mâcloskey et al. "The actively controlled jet in crossflow". In: *Journal of Fluid Mechanics* (2002).

[21] H Johari, M Pacheco-Tougas, and JC Hermanson. "Penetration and mixing of fully modulated turbulent jets in crossflow". In: *AIAA journal* (1999).

[22] Hans H Bruun. "Hot-wire anemometry: principles and signal analysis". In: *Measurement Science and Technology* (1996).

[23] https://www.sfu.ca/~mbahrami/ENSC%20388/Notes/Natural%20Convection.pdf.

[24] Hajime Nakamura, Naoki Shiibara, and Shunsuke Yamada. “Quantitative measurement of spatio-temporal heat transfer to a turbulent water pipe flow”. In: *International Journal of Heat and Fluid Flow* (2017).

[25] Martin Dostál, Karel Petera, and Stanislav Solnař. “Gnielinskiâs correlation and a modern temperature-oscillation method for measuring heat transfer coefficients”. In: *EPJ Web of Conferences*. EDP Sciences. 2022.

[26] C. Lautenberger et al. “Radiation Heat Transfer”. In: Springer New York, 2016.

[27] https://assets.testequity.com/te1/Documents/ARTICLE_LIBRARY/FLIR-IR-Thermography_How-It-Works.pdf.

[28] https://site.unibo.it/ciclope/en/other-facilities/copy_of_the-long-pipe.

[29] https://www.metalwork.it/.

[30] https://www.smc.eu/en-eu.

[31] https://www.ni.com.

[32] AFM Torre et al. “Evaluation of anisotropic tangential conduction in printed-circuit-board heated-thin-foil heat flux sensors”. In: *International Journal of Heat and Mass Transfer* (2018).

[33] https://www.flir.eu/products/t560/?vertical=condition%20monitoring&segment=solutions.

[34] https://www.honeywell.com.

[35] https://www.mks.com/.

Acknowledgements

Vorrei tutte le persone che hanno reso possibile il raggiungimento di questo importante traguardo.
Partendo con i ringraziamenti ufficiali, vorrei ringraziere il relatore Gabriele Bellani e il correlatore Lorenzo Magnagni, un grazie anche a tutti i ragazzi del CICLoPE.
Un grazie speciale ai miei genitori che mi hanno reso cio che sono oggi e che mi hanno sempre sostenuto e mai fatto mancare il loro supporto.
Un immenso grazie a Stefania, che e sempre stata al mio fianco e mi ha supportato nei momenti piu duri. Mi rendi felice grazie per cio che sei.
Un grazie anche agli amici di una vita, la nostra amicizia e' una cosa speciale e senza di voi questi anni e questo percorso non sarebbero stati cosi belli.